
Unterschrift Betreuer



TECHNISCHE
UNIVERSITÄT
WIEN
Vienna University of Technology

DIPLOMARBEIT

Strong field induced charge transfer in bulk insulators

ausgeführt am Institut für Theoretische Physik
der Technischen Universität Wien

unter der Anleitung von

Associate Prof. Dipl.-Ing. Dr. techn. Christoph Lemell

durch

Wolfgang Moser

Margaretengürtel 144/22,

1050 Wien

May 13, 2016

Unterschrift Student

Abstract

The rapid improvement of laser technology in the last decades enables scientists to explore ever shorter timescales of physical processes. Waveform controllable ultra-short high-intensity laser pulses can be utilized to investigate electron motion on the subfemtosecond timescale in atoms, molecules, and even solid matter.

A promising branch for new technologies of this so-called field of attosecond physics is summarized by the term “lightwave electronics” based on the controlled steering of electrons by light oscillations with the vision of realizing electronic devices operating with clock speeds orders of magnitude faster than present conventional semiconductor devices. By investigating the micro- and macroscopic charge transfer occurring in bulk insulators this work aims at increasing the understanding of the underlying physics.

The involved quantum mechanical processes are modelled by ab-initio simulations based on time-dependent density functional theory for two materials, diamond and α -quartz. This microscopic model is coupled to the macroscopic regime by combining time-dependent functional theory with Maxwell’s equations. Furthermore, a semiclassical model, intended to support the interpretation of the quantum mechanical results, is presented. Whereever possible, the results are compared to existing experimental findings.

These models are applied to strong ultra-short laser pulses interacting with α -quartz and diamond in single cell and macroscopic simulations. A strong dependence of the amount of transferred charge on the carrier-envelope phase is found and explained by the semiclassical model. Investigating effects of symmetry breaking due to laser fields composed of two colors reveal strong variations of the amount of transferred charge as a function of the phase relation of the two pulses as well.

These results open the pathway to designing ultra-fast light-driven switching devices for future petahertz electronics. Moreover, the applicability of time-dependent density functional theory to obtain an accurate description of the involved process can be confirmed.

Kurzfassung

Die rasante Verbesserung der Lasertechnologie in den letzten Jahrzehnten ermöglicht es Wissenschaftlern physikalische Prozesse auf immer kürzeren Zeitskalen zu erforschen. Ultrakurze hochintensive Laserpulse, deren Wellenform kontrollierbar ist, können dazu verwendet werden Elektronenbewegungen auf der Subfemtosekundenzeitskala in Atomen, Molekülen bis hin zu Festkörpern zu untersuchen.

Ein vielversprechender Zweig für neue Technologien dieser sogenannten Attosekundenphysik wird zusammengefasst unter dem Begriff "Lichtwellenelektronik", der auf der kontrollierten Steuerbarkeit von Elektronen durch Lichtoszillationen basiert und auf die Vision der Realisierung von elektronischen Geräten mit Größenordnungen höheren Taktraten als herkömmliche Halbleiterbauelemente hinweist. Anhand der Untersuchung des in Isolatoren auftretenden mikro- und makroskopischen Ladungstransfers versucht diese Arbeit das Verständnis der zugrundeliegenden Physik zu verbessern.

Die beteiligten quantenmechanischen Prozesse werden für zwei Materialien, Diamant und α -Quarz, durch ab-initio Simulationen untersucht, die auf zeitabhängiger Dichtefunktionaltheorie beruhen. Dieses mikroskopische Modell ist an das makroskopische Regime durch die Kombination mit den Maxwellgleichungen gekoppelt. Weiters wird ein semiklassisches Modell präsentiert, das darauf abzielt die Inter-

pretation der quantenmechanischen Ergebnisse zu erleichtern. Soweit verfügbar, werden die Resultate mit vorhandenen experimentellen Daten verglichen.

Die Modelle werden angewendet, um die Wechselwirkung von ultra-kurzen Laserpulsen mit den Materialien in einzelnen Elementarzellen und in makroskopisch ausgedehnten Kristallen zu beschreiben. Eine starke Abhängigkeit der transferierten Ladung von der Träger-Einhüllenden-Phase wurde gefunden und kann anhand der semiklassischen Simulation erklärt werden. Außerdem werden die durch Symmetriebrechung mittels eines zweifarbigem Laserfeldes induzierten Effekte studiert. Hier kann ebenso eine erhebliche Variation der transferierten Ladung als Funktion der Phasenbeziehung der beiden Pulse gefunden werden.

Diese Resultate tragen zur Entwicklung von ultraschnellen lichtgesteuerten Schaltergeräten für zukünftige Petahertzelektronik bei und untermauern die Anwendbarkeit von zeitabhängiger Dichtefunktionaltheorie um eine präzise Beschreibung der beteiligten Prozesse zu erlangen.

Contents

Introduction	1
1 Theory	3
1.1 Density functional theory	4
1.1.1 Adaption and implementation	7
1.2 Time-dependent density functional theory	8
1.2.1 Adaption and implementation	9
1.3 Multiscale model (Maxwell+TDDFT)	11
1.4 Semiclassical model	13
2 Materials	19
2.1 Diamond	19
2.1.1 Ground state properties	21
2.1.2 Linear response	24
2.2 α -Quartz (SiO_2)	26
2.2.1 Ground state properties	27
2.2.2 Linear response	29

3	Single crystal unit cells	33
3.1	Single color laser pulses	33
3.2	Two-color laser pulses	39
3.3	Semiclassical estimate	44
4	Multiscale coupled dynamics	47
5	Conclusions and outlook	55
	Acknowledgments	57
	Bibliography	i

Introduction

The advent of laser sources providing strong ultra-short few-cycle laser pulses with intensities up to 10^{14} W/cm² has opened up a completely new field of research, the time-resolved spectroscopy of electronic processes on their natural (sub-)femtosecond timescale. Experimental findings for solid dielectric targets point to the possibility of designing ultrafast electro-optical switches aiming at increasing the operation speeds of electronic signal processing up to the petahertz-regime [1]. In this work laser-solid interactions are simulated using time-dependent functional theory (TDDFT) and semiclassical simulations to add to the understanding of ultrafast electronic processes in dielectrics. In particular, the interest lies in the effects induced by breaking the crystal symmetry with the laser electric field, i.e. by variation of the carrier-envelope phase for ultrashort pulses or by adding a second phase-shifted laser pulse with different oscillation frequency.

Where available, experimental results are compared to the simulated results. Semiclassical calculations performed within this work help to characterize the underlying physical mechanisms at very low computational cost.

In the first chapter a brief overview of the theoretical framework is given. Static density functional theory (DFT) will act as the starting point for all time-dependent simulations based on TDDFT. The description of the macroscopic

extension to couple TDDFT with Maxwell's equations will finalize this chapter. In chapter two the results of the ground-state calculations for both investigated materials, diamond and α -quartz, are presented. The computed observables are compared to experimental values to assess the accuracy of the presented methods. The third chapter discusses results of the time-dependent simulation of single crystal unit cells. Starting with single color lasers, the dependence of the charge transferred within the unit cell on the carrier-envelope phase and the intensity is studied. Subsequently, a weak second color pulse is superimposed on the primary laser pulse and the impact of varying the relative phase of these pulses is investigated. Finally, the previously mentioned semiclassical model is described and its results are compared to the fully quantum mechanical data. At the end of this thesis coupled micro- and macroscopic simulations are discussed in which the charge deposition depending on the penetration depth of the electromagnetic field is explored.

Unless stated differently, atomic units ($e = \hbar = m_e = 1$) are used. All 2D and 3D visualizations of crystal structures including charge density plots were performed with VisIt [2]. This work used computational resources of the Vienna Scientific Cluster (VSC) and the K computer provided by the RIKEN Advanced Institute for Computational Science.

1 Theory

The simulation of highly intense short laser pulses irradiating solids requires various approximations which, however, must not obscure the detailed physical processes behind the observed phenomena. For instance the motion of atomic nuclei can be safely ignored since their oscillation periods around their ground-state positions are usually larger than the duration of the laser pulse. Another approximation valid at low laser intensities is linear response theory in which a response linear in the exciting electric field is assumed. High intensity pulses, though, drive strong nonlinear optical processes which are at the core of many of the topics currently studied such as high harmonic generation, attosecond metrology, or lightwave electronics [3].

In principle, the many-particle time-dependent Schrödinger equation has to be solved numerically in order to describe such nonlinear processes. This approach has been successfully followed for helium but is far from feasible for more than two active electrons.

The following sections provide a short introduction to the theoretical models used to describe the investigated environments. At the core of these methods is time dependent density functional theory (TDDFT) which will be explained in section 1.2. A real-space, real-time implementation of TDDFT for the simulation

of laser pulses irradiating solids has been developed by Yabana et al. [4]. This implementation was used for all TDDFT calculations conducted in the context of this thesis. At the end of each of the following sections, specific details and extensions of the particular implementation are presented.

1.1 Density functional theory

A well-known and widely used approximation to overcome the limitations encountered by the many-body problem is density functional theory (DFT) developed by Hohenberg and Kohn in 1964 [5]. Two theorems were proposed in this publication. The first Hohenberg-Kohn theorem establishes a one-to-one correspondence between the external potential $V(\mathbf{r})$ and the ground-state density $n_0(\mathbf{r})$ linking all ground-state properties in a many-electron system to its ground-state particle density. Furthermore, this theorem shows that the ground-state particle density is associated with a unique ground-state wave function Ψ_0 , thereby reducing the number of variables from $3N$ in $\Psi(\mathbf{r}_1, \dots, \mathbf{r}_N)$ to 3 in $n(\mathbf{r})$, where N is the number of particles in the system.

Subsequently, in 1965, Kohn and Sham [6] were able to map the system of N interacting electrons with wave function $\Psi(\mathbf{r}_1, \dots, \mathbf{r}_N)$, described by the static Schrödinger equation

$$H\Psi_j(\mathbf{r}_1, \dots, \mathbf{r}_N) = E_j\Psi_j(\mathbf{r}_1, \dots, \mathbf{r}_N), \quad (1.1)$$

onto a system of N non-interacting single-particle pseudo wave functions in an

external potential. The resulting Kohn-Sham equations,

$$\left(-\frac{\nabla^2}{2} + V_s[n](\mathbf{r})\right) \varphi_j(\mathbf{r}) = \varepsilon_j \varphi_j(\mathbf{r}), \quad (1.2)$$

provide a self-consistent method to obtain the density of a many electron system from the solved Kohn-Sham orbitals $\varphi_j(\mathbf{r})$ of Equation 1.2,

$$n_0(\mathbf{r}) = \sum_{j=1}^N |\varphi_j(\mathbf{r})|^2. \quad (1.3)$$

In Equation 1.2 the local external potential of the non-interacting system is defined as

$$V_s[n](\mathbf{r}) = V(\mathbf{r}) + \int d\mathbf{r}' \frac{n(\mathbf{r}')}{|\mathbf{r} - \mathbf{r}'|} + V_{XC}[n], \quad (1.4)$$

with the external potential $V(\mathbf{r})$ of the interacting system, the Coulomb potential and the exchange-correlation (XC) potential $V_{XC}[n]$. The XC potential,

$$V_{XC}[n] = \frac{\delta E_{XC}[n]}{\delta n(\mathbf{r})}, \quad (1.5)$$

is the functional derivative of the XC energy, which contains the electron-electron interaction and the difference of the kinetic energies of the real interacting system and the fictitious non-interacting system.

The Kohn-Sham equations provide a formally exact quantum mechanical description of the system but exact formulations of the exchange-correlation potential exist only for the free electron gas and therefore approximations are used to describe the many particle interactions. In the widely used and oldest approximation, the local density approximation (LDA) [6, 7] the XC energy is expressed

by

$$E_{XC}^{LDA}[n] = \int d\mathbf{r} \bar{n} \varepsilon_{XC}(\bar{n}), \quad (1.6)$$

valid for a free electron gas. Instead of the constant charge density \bar{n} one inserts the local electron density $n(\mathbf{r})$. The XC potential is then obtained from $V_{XC}^{LDA}[n] = \delta E_{XC}^{LDA}[n] / \delta n(\mathbf{r})$. For densities slowly varying in space, this approach should give good results. It turns out, however, that also for systems with large density gradients (e.g. atoms) LDA works well. For dielectrics, LDA is known to underestimate band gap energies which are of major importance in many applications.

Better approximations for XC functionals depend not only on the local density itself but also on its (higher order) gradients. Another popular choice are therefore so-called generalized gradient approximations (GGA), heuristic approaches for the dependence of $V_{XC}[n]$ on the density gradients. Their performance is judged by how well they satisfy the exact properties of the XC energy density. For even higher accuracy than GGA, meta-GGA potentials have been derived which additionally include the Laplacians of the density and the orbital kinetic energy densities. A recently proposed meta-GGA is the Tran-Blaha modified Becke-Johnson (TB-mBJ) XC potential [8]. It reduces the error in the band gap energies and introduces a free parameter c correlated with the band gap. This is achieved by using LDA correlation [9] and a modification of the Becke-Johnson exchange potential [10],

$$V_X^{TB-mBJ}(\mathbf{r}) = V_X^{BR}(\mathbf{r}) + (3c - 2) \frac{1}{\pi} \sqrt{\frac{5}{12}} \sqrt{\frac{2t(\mathbf{r})}{n(\mathbf{r})}}. \quad (1.7)$$

Here, $V_X^{BR}(\mathbf{r})$ is the Becke-Roussel potential [11] and $t(\mathbf{r})$ is the kinetic energy

density. For $c = 1$ the original Becke-Johnson potential is recovered.

1.1.1 Adaption and implementation

The system under investigation in this thesis is a bulk solid target which is described as an infinitely extended periodic crystal. To find the ground-state distribution of electrons within this crystal the corresponding static Kohn-Sham equations,

$$\varepsilon_j \varphi_j(\mathbf{r}) = \underbrace{\left(\frac{1}{2} \mathbf{p}^2 + V_{ion}(\mathbf{r}) + \int d\mathbf{r}' \frac{n(\mathbf{r}')}{|\mathbf{r} - \mathbf{r}'|} + V_{XC}[n] \right)}_{H_{KS}} \varphi_j(\mathbf{r}), \quad (1.8)$$

have to be solved. In Equation 1.8 \mathbf{p} is the momentum operator and $V_{ion}(\mathbf{r})$ is the crystal lattice potential. Only valence band electrons are propagated, interaction with deeply bound core electrons is accounted for by a norm-conserving pseudopotential $V_{ion}(\mathbf{r})$ of the Troullier and Martins form [12].

Due to the preserved lattice periodicity of the Hamiltonian, $H_{KS}(\mathbf{r} + \mathbf{R}) = H_{KS}(\mathbf{r})$ with \mathbf{R} being a linear combination of the three unit cell vectors, the Bloch theorem can be applied to the orbital wave functions. Accordingly, the wave function can be split into a plane wave modulated by a periodic function,

$$\varphi_j(\mathbf{r}) = e^{i\mathbf{k}\mathbf{r}} u_{n,\mathbf{k}}(\mathbf{r}), \quad (1.9)$$

with n and \mathbf{k} being the band index and the crystal momentum, respectively. The combination of n and \mathbf{k} is the orbital index j . This approach allows to only solve the Kohn-Sham equations for a single crystal unit cell instead of the full solid.

The static Kohn-Sham equations are solved self-consistently by applying a conjugate gradient minimization for the total energy. Numerically, the derivatives of

the orbital wave functions are computed using high-order finite difference formulas [13]. A nine point stencil is used for both the first and second derivatives.

1.2 Time-dependent density functional theory

The processes investigated in this work are obviously not static, requiring a theoretical method to describe the time evolution of the systems that are considered. Time dependent density functional theory (TDDFT) was first introduced by Runge and Gross in 1984 [14]. The Runge-Gross theorem is the time-dependent analogue of the first Hohenberg-Kohn theorem and states that two densities $n(\mathbf{r}, t)$ and $n'(\mathbf{r}, t)$ evolving from the same initial state ψ_0 in two different potentials $V(\mathbf{r}, t)$ and $V'(\mathbf{r}, t)$ will become different immediately after the evolution starts. Hence, for any initial state a one-to-one correspondence between time-dependent densities and potentials exists. This very fundamental insight leads to the fact that both the many-body Hamiltonian $H(t)$ and the many-body wave function $\Psi(t)$ are functionals of the time-dependent density $n(\mathbf{r}, t)$. Later, the justification to represent the interacting system by a non-interacting equivalent (the time-dependent Kohn-Sham approach) was given by van Leeuwen in 1999 [15]. This leads to the time-dependent Kohn-Sham equations (TDKS),

$$\left(-\frac{\nabla^2}{2} + V_s[n](\mathbf{r}, t)\right) \varphi_j(\mathbf{r}, t) = i\partial_t \varphi_j(\mathbf{r}, t), \quad (1.10)$$

with the initial state

$$\varphi_j(\mathbf{r}, t_0) = \varphi_j^0(\mathbf{r}) \quad (1.11)$$

obtained from the solution of the static Kohn-Sham equations. The time-dependent density is then given by

$$n(\mathbf{r}, t) = \sum_{j=1}^N |\varphi_j(\mathbf{r}, t)|^2, \quad (1.12)$$

which can be used to calculate the physical observables of interest which are also functionals of this density.

As in DFT, the most important unknown in TDDFT is the time-dependent XC potential $V_{XC}[n(\mathbf{r}, t)]$. To exploit the vast knowledge from DFT accumulated over decades the static XC potential is also used with the time-dependent density $n(\mathbf{r}, t)$ in most cases:

$$V_{XC}^A[n] = V_{XC}^0[n_0]|_{n_0(\mathbf{r}) \rightarrow n(\mathbf{r}, t)} \quad (1.13)$$

This approximation is known as the adiabatic approximation where the term “adiabatic” refers to the assumption of slowly varying changes in the external potential and the induced change.

For a thorough introduction to the methods of TDDFT see, e.g., [16].

1.2.1 Adaption and implementation

The crystal is exposed to a spatially uniform but time dependent electric field $\mathbf{F}(t)$ derived from the vector potential $\mathbf{A}(t) = -c \int_{-\infty}^t \mathbf{F}(t') dt'$. The side lengths of unit cells in solids are several orders smaller than typical laser wavelengths of a few hundreds of nanometers. Therefore, the long wavelength limit is applicable in this case which justifies the approximation of a spatially uniform electric field within a unit cell.

After the ground-state calculation is converged the electronic system is propa-

gated according to the TDKS equations which are given in the length gauge via

$$i\partial_t\varphi_j(\mathbf{r},t) = \left(\frac{1}{2}\mathbf{p}^2 + V_{ion}(\mathbf{r}) + \int d\mathbf{r}' \frac{n(\mathbf{r},t)}{|\mathbf{r}-\mathbf{r}'|} + V_{XC}(\mathbf{r},t) + \mathbf{F}(t)\cdot\mathbf{r} \right) \varphi_j(\mathbf{r},t), \quad (1.14)$$

where the last term of the Hamiltonian describes the electron-laser field interaction in dipole approximation.

The linear laser field term on the right-hand side of Equation 1.14, however, destroys the spatial periodicity of the orbitals. To circumvent this problem, the Kohn-Sham equations are transformed to the velocity gauge by

$$\tilde{\varphi}_j(\mathbf{r},t) = \exp \left[i \frac{1}{c} \mathbf{A}(t) \cdot \mathbf{r} \right] \psi_j(\mathbf{r},t). \quad (1.15)$$

Inserting Equation 1.15 into Equation 1.14 gives the Kohn-Sham equations in the velocity gauge,

$$H_{KS} = \frac{1}{2} \left(\mathbf{p} + \frac{1}{c} \mathbf{A}(t) \right)^2 + V_{ion}(\mathbf{r}) + \int d\mathbf{r}' \frac{n(\mathbf{r},t)}{|\mathbf{r}-\mathbf{r}'|} + V_{XC}(\mathbf{r},t) \quad (1.16)$$

$$i\partial_t\psi_j(\mathbf{r},t) = H_{KS}\psi_j(\mathbf{r},t), \quad (1.17)$$

which conserves the lattice periodicity and allows to model the time evolution within one single unit cell by solving the TDKS equations with periodic boundary conditions. The resulting TDKS Equations 1.17 are solved using a fourth-order Taylor expansion of the time evolution operator [4, 17],

$$\exp^{-iH_{KS}\Delta t} \approx \sum_{n=0}^4 \frac{(i\Delta t)^n}{n!} H_{KS}^n \quad (1.18)$$

with very small time steps of $\Delta t \approx 0.01$ a.u.

1.3 Multiscale model (Maxwell+TDDFT)

Although the single crystal cell simulations are able to explain many experimental observations fairly well, (macroscopic) propagation effects appearing in real solids are neglected. For high intensities the propagation of the laser pulse inside the material is strongly influenced by the non-linear response of the electronic system. The feedback of the electron dynamics to the electric field involves phenomena on two different spatial and temporal scales: The carrier wavelength of the laser pulse is on the order of a few hundreds of nanometers whereas the motion of electrons inside a crystal cell induced by this pulse happens on the nanometer scale. Therefore, a distinct treatment is necessary and leads to the multiscale approach [4] explained in the following.

While the principle TDDFT method described previously is kept for the description of the microscopic electron dynamics a coupling to the macroscopic Maxwell equations is introduced. As a consequence two different spatial grids have to be employed using a one-dimensional macroscopic coordinate R and microscopic coordinates \mathbf{R} around each macroscopic position R .

In Fig. 1.1 the basic geometry of the simulation is sketched. It illustrates the macroscopic system with a laser pulse irradiating a crystalline material. Outside the crystal the pulse is assumed to travel through vacuum. At each of the macroscopic grid points within the solid a single cell TDDFT calculation is performed (see the inset in Fig. 1.1). The grid points are coupled by Maxwell's equations. For the sake of simplicity the propagation is limited to one dimension along the surface

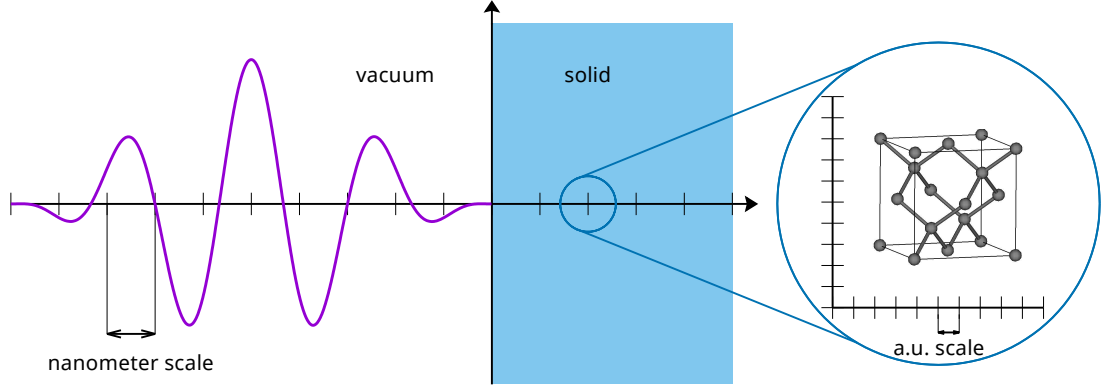


Figure 1.1: Geometry of the multiscale simulation.

normal of the bulk solid. The vector potential $A_R(t)$ at each point R follows the one-dimensional wave equation,

$$\left(\frac{1}{c^2} \frac{\partial^2}{\partial t^2} - \frac{\partial^2}{\partial R^2} \right) A_R(t) = -\frac{4\pi}{c} J_R(t), \quad (1.19)$$

where $J_R(t)$ is the macroscopic current at point R . Due to the restriction to one dimension the macroscopic simulation works only for symmetric targets. Therefore, orientations of materials which induce currents in directions other than the laser polarization direction cannot be treated at the moment. The current $J_R(t)$ is typically non-zero for points inside the crystal and its magnitude is determined by the solution of the time-dependent Kohn-Sham equations at each site. An index R indicating the macroscopic coordinate is added to the TDKS,

$$\begin{aligned} i\partial_t \psi_{j,R}(\mathbf{r}, t) = & \left(\frac{1}{2} \left[\mathbf{p} + \frac{1}{c} \hat{\mathbf{e}} A_R(t) \right]^2 + V_{ion}(\mathbf{r}) \right. \\ & \left. + \int d\mathbf{r}' \frac{n_R(\mathbf{r}, t)}{|\mathbf{r} - \mathbf{r}'|} + V_{XC}(\mathbf{r}, t) \right) \psi_{j,R}(\mathbf{r}, t), \end{aligned} \quad (1.20)$$

with $\hat{\mathbf{e}}$ being the laser polarization direction. From the microscopic density,

$$n_R(\mathbf{r}, t) = \sum_{j=1}^N |\psi_{j,R}(\mathbf{r}, t)|^2, \quad (1.21)$$

the micro- and macroscopic currents can be obtained,

$$\mathbf{j}_R(\mathbf{r}, t) = \sum_{j=1}^N \frac{1}{2} \left[\psi_{j,R}^*(\mathbf{r}, t) \left(-i\nabla_{\mathbf{r}} + \frac{1}{c} \hat{\mathbf{e}} A_R(t) \right) \psi_{j,R}(\mathbf{r}, t) + \text{c.c.} \right] \quad (1.22)$$

$$J_R(t) = \frac{1}{\Omega} \int_{\Omega} d\mathbf{r} \hat{\mathbf{e}} \mathbf{j}_R(\mathbf{r}, t). \quad (1.23)$$

The vector potentials $A_R(t)$ at the macroscopic grid points R inside the crystal are calculated from Equation 1.19 and then used in Equation 1.20 to obtain the currents $J_R(t)$ which are eventually fed back to Equation 1.19 where they are used in the calculation of the next time step. As described in subsection 1.2.1 the vector potential $A_R(t)$ is treated as spatially uniform within a microscopic cell.

In order to solve the macroscopic wave equation, both, the spatial and the time derivatives are approximated using a three-point approximation,

$$\begin{aligned} A_R(t + \Delta t) &= 2A_R(t) - A_R(t - \Delta t) \\ &+ \left(\frac{c\Delta t}{\Delta R} \right)^2 [A_{R+\Delta R}(t) - 2A_R(t) + A_{R-\Delta R}(t)] \\ &- 4\pi c \Delta t^2 J_R(t) \end{aligned} \quad (1.24)$$

1.4 Semiclassical model

Since single cell TDDFT calculations can only be performed on supercomputers, computationally cheaper estimates are desired. In order to capture the most

important quantum-mechanical processes a semiclassical trajectory Monte-Carlo simulation was set up and is described in the following.

For atoms two regimes of dominating ionization processes can be distinguished: multi-photon and tunneling ionization. The transition from the multi-photon excitation regime to the tunnel excitation regime is governed by the Keldysh parameter [18]

$$\gamma = \frac{\omega}{F_0} \sqrt{2\Delta}, \quad (1.25)$$

where ω is the laser frequency, F_0 denotes the peak laser field and Δ the width of the band gap. For $\gamma \gg 1$ multi-photon excitation dominates while $\gamma \ll 1$ indicates tunnel ionization.

At low intensities ($\gamma \gg 1$) photoionization can occur if the atom absorbs N photons of energy $\hbar\omega$ from the laser pulse with a total energy large enough to cover the band gap Δ , $N\hbar\omega \geq \Delta$ (Fig. 1.2). The ionization rate for N -photon ionization is given by

$$\Gamma_N(t) \propto I(t)^N, \quad (1.26)$$

where I is the intensity of the laser field envelope.

At high intensities ($\gamma \ll 1$) tunnel ionization dominates. The tunneling process can be outlined as follows: The presence of an alternating electric field distorts the potential landscape of an atom (Fig. 1.3). Alternately, one side of the atomic potential well is lowered and electrons from the highest occupied state may tunnel through the barrier. As long as the Keldysh parameter is sufficiently small ($\gamma < 1/2$, [19]) the so-called ADK model (Ammosov-Delone-Krainov) [20] is applicable

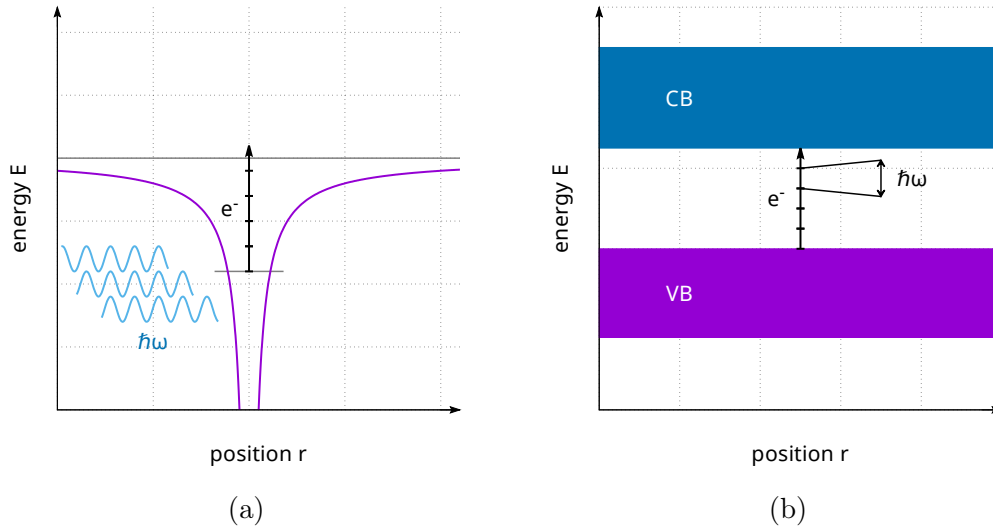


Figure 1.2: With small probability $\propto I(t)^N$ the atom may absorb N photons from the laser pulse leading to ionization in (a) the atomic case, (b) the solid case.

and gives an expression for the tunnel ionization rate,

$$\Gamma_{ADK}(t) \propto |F(t)|^{\frac{3}{2}-2n^*} \exp\left(-\frac{2(2\Delta)^{\frac{3}{2}}}{3|F(t)|}\right), \quad (1.27)$$

where $F(t)$ is the time-dependent electric field strength and $n^* = Z/\sqrt{2W}$ is the effective quantum number with the charge Z of the atomic residue.

For this semiclassical model only relative ionization rates are important and therefore normalized rates are used in both cases. Although being derived for electron ionization in atoms, the ionization process in solids is assumed to follow the same rate equations (Fig. 1.3 and Fig. 1.2).

In Fig. 1.4 the two possible rates along with their integrals and the electric field are shown for a strong laser pulse. Using these ionization rates a large number of electrons is simulated. The time of creation t_0 of each ionized electron is selected

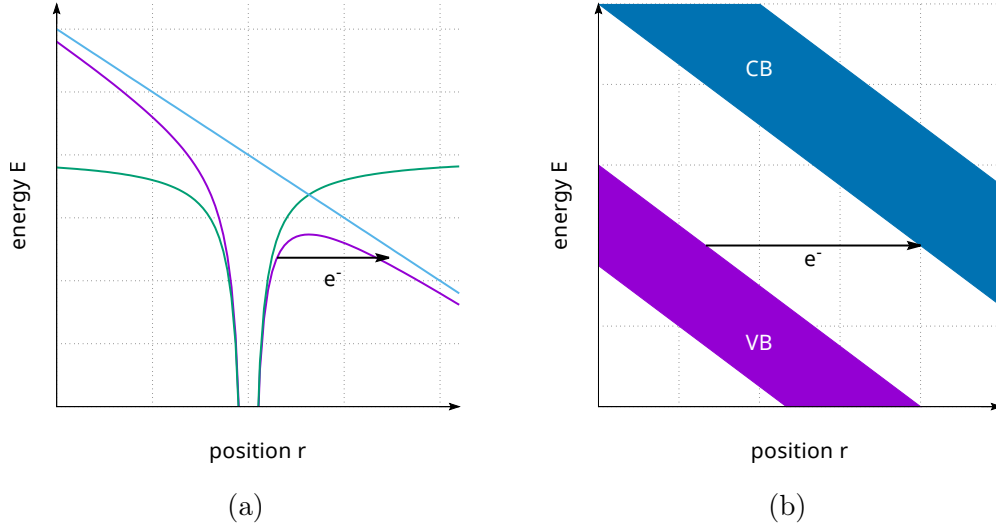


Figure 1.3: Tunnel ionization process: The electric field distorts the potential landscape and induces a finite probability for an electron to be ionized. (a) the atomic case, (b) the solid case.

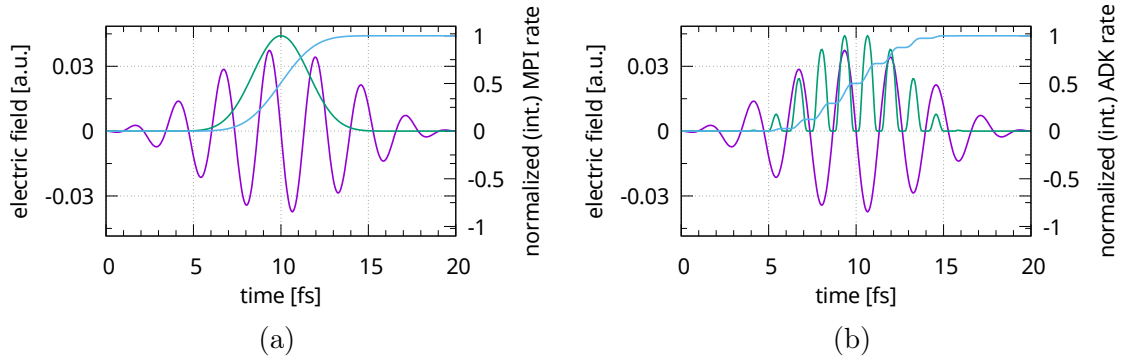


Figure 1.4: Normalized (green curve) and integrated (blue curve) ionization rates for the two different ionization mechanisms along with the laser field $F(t)$ (purple curve). (a) multi-photon ionization $\Gamma_N(t) \propto I(t)^N$, (b) tunnel ionization $\Gamma_{ADK}(t) \propto \exp(-|F(t)|^{-1})$.

from the probability distributions for tunneling or multi-photon ionization. In the case of high intensities, the starting location of the electron propagation is given by the tunneling distance $r_0 = W/F(t_0)$. For multi-photon excitations the starting location is $r_0 = 0$. The simulation is performed in one dimension and the crystal potential is approximated as

$$V_{ion}(r) = \Delta V \cos\left(\frac{2\pi}{\lambda_{ion}}r\right), \quad (1.28)$$

where ΔV and λ_{ion} are extracted from the TDDFT simulations. For periodic crystal directions λ_{ion} is given by the spacing of atoms. ΔV characterizes the remaining screened potential that the ionized electron experiences while propagating through the crystal. Possible upper limits for the choice of ΔV are the average of the Kohn-Sham potential V_s (Equation 1.4) or the band gap energy Δ .

The electrons are then propagated within the remaining laser field and the ionic potential by an adaptive stepsize fourth-order Runge-Kutta method according to the Newtonian equation of motion,

$$\ddot{r}(t) = F(t) - \frac{\partial V_{ion}(r)}{\partial r}, \quad (1.29)$$

with an initial velocity of $v_0 = 0$.

To estimate the net amount of charge transferred within the crystal the directions of propagation of the electrons after the conclusion of the laser pulse can be used (left/right asymmetry). The ratio of electrons moving in positive direction to those moving in negative direction, $Q = N_+/N_-$, is a direct indication of the amount of transferred charge.

2 Materials

Prior to the description of the main investigations, a brief overview of the materials used in the calculations and the static DFT results is given. In this study the focus lies on two materials, diamond and SiO_2 in the form of α -quartz. As diamond requires much less computational resources due to its high symmetry, most of the results presented in the subsequent chapters were acquired for this material. SiO_2 , however, has been studied many times before and more experimental results are available for comparison. In addition, the asymmetric crystal structure of SiO_2 causes interesting physical phenomena such as, e.g., the nonlinear photogalvanic effect [21]. In the following, the ground-state properties of diamond and SiO_2 as well as computational details important for the interpretation of the time-dependent results presented in chapter 3 and chapter 4 are introduced. All calculations were performed on the Vienna Scientific Cluster.

2.1 Diamond

As diamond was the first known example of a face-centered cubic Bravais lattice with two basis atoms at $(0, 0, 0)$ and $(\frac{a_0}{4}, \frac{a_0}{4}, \frac{a_0}{4})$, its crystal structure has been named the “diamond structure” Other known materials with diamond structure

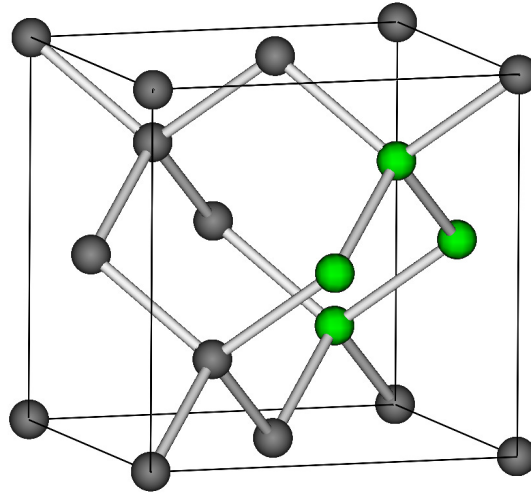


Figure 2.1: Diamond crystal structure. The 4 carbon atoms in the unit cell are highlighted in green.

like zinc selenide have two different atoms in their basis. In this case the structural pattern is called the “zincblende structure”.

Apart from translational symmetry which reduces the information of the reciprocal space to the first Brillouin zone, the diamond structure also features symmetries under rotations, inversions, and reflections. The first Brillouin zone shows in total 48 point symmetries (space group $Fd\bar{3}m$). In the presence of an external electromagnetic field, however, symmetries involving the polarization direction break. Therefore a total of 8 symmetry operations are left which together with the requirement of the TDDFT code for a cuboid unit cell lead to the choice of the unit cell atoms depicted in Fig. 2.1.

The size of the unit cell is $2.52 \text{ \AA} \times 2.52 \text{ \AA} \times 3.57 \text{ \AA}$ [22]. Each of the 4 unit cell atoms has 4 valence electrons and therefore a total of 16 valence electrons are

considered in the calculations. In order to achieve the full possible occupancy of 2 electrons per valence band, 16 bands are included in the simulation to account for the known lowering of the occupancy of the energetically highest bands. In real space a $16 \times 16 \times 20$ grid is used, whereas the reciprocal grid has $20 \times 20 \times 16$ points. These settings were used throughout all diamond calculations unless stated differently. The results of the ground-state simulation are described in the following section.

2.1.1 Ground state properties

For diamond two different XC potential approximations were tested and evaluated. The first and computationally cheaper choice was LDA [7]. This potential is known to underestimate the bandgap energies of insulators. The calculations yielded a band gap energy of $\Delta_{LDA} = 4.33 \text{ eV}$. Secondly, the TB-mBJ XC potential was employed. The free parameter c was varied until a band gap value close to the experimental value was reached. With $c = 1.28$ a band gap of $\Delta_{TB-mBJ} = 5.46 \text{ eV}$ was found which is close to the experimental value of $\Delta \approx 5.4 \text{ eV}$ [23]. As many investigated observables sensitively depend on the precise value of the excitation gap only results using the TB-mBJ XC potential are discussed in the following.

Typically, a conjugate gradient minimization is performed to obtain the ground state, converging after approximately 150 iterations with a ground state energy of $E_{GS} = -618.9 \text{ eV}$. The computation was performed using 5 computational nodes (each having 2 processors with 8 cores) with a total computation time of less than 2 min. In Fig. 2.2 an example for the convergence process during the ground state calculation is depicted. After about 80 iterations approximate convergence is

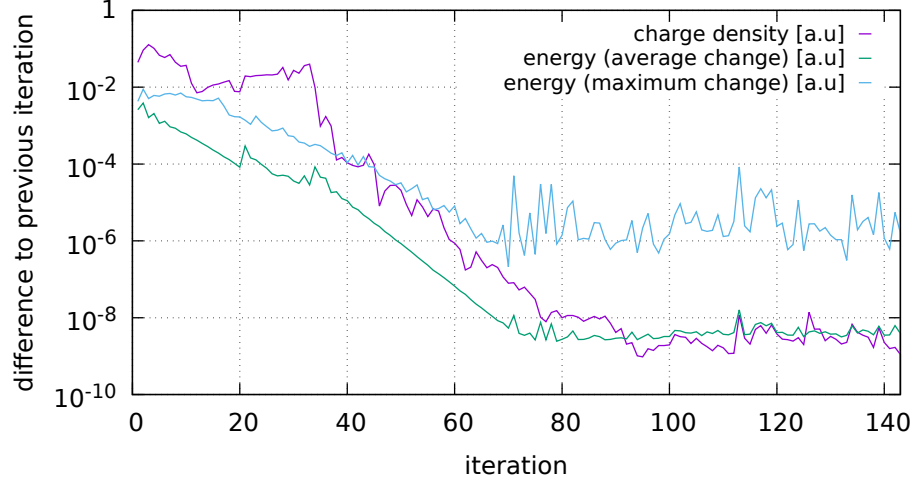


Figure 2.2: Ground state convergence process for diamond showing the per-iteration change of the charge density as well as the average and the maximum change of the energy per \mathbf{k} -point.

reached. The procedure stops as soon as the relative change in charge density and energy stays below a predefined threshold for 4 iterations. Nevertheless, significant variations at the end of the calculation may still remain due to the finite grid spacing in real and reciprocal space.

In Fig. 2.3 the occupied and unoccupied ground-state densities of states as compared to experimental results [24] are shown. Excellent agreement over the complete valence band is achieved. The agreement in the conduction band is reduced due to the smaller band gap of $\Delta \approx 4.1$ eV in the experimental data.

Figure 2.4 shows the ground state electron density extracted from the Kohn-Sham orbitals $\psi_i(\mathbf{r}, t)$

$$n(\mathbf{r}, t) = \sum_i |\psi_i(\mathbf{r}, t)|^2. \quad (2.1)$$

As expected, the formation of bondings between carbon atoms is observable. The

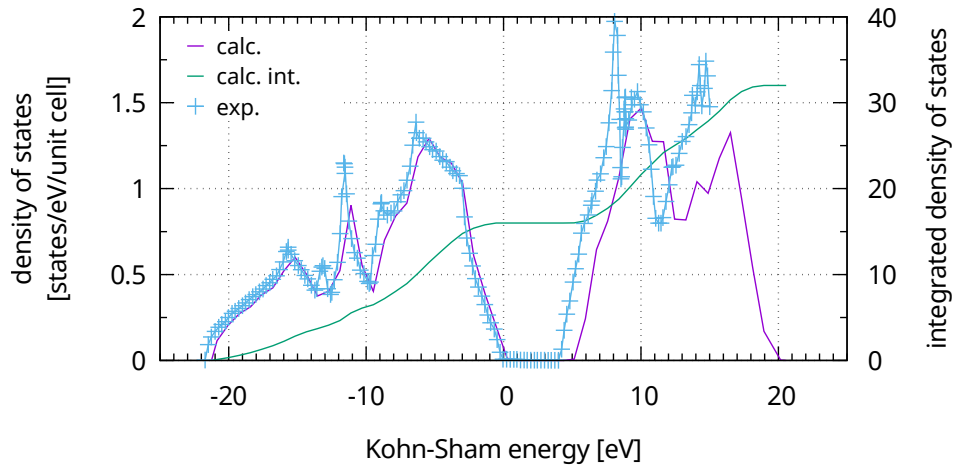


Figure 2.3: Ground state density of states (calculated and experimental [24]) and integrated density of states for diamond. The zero-point on the energy scale is defined as the top of the valence band.

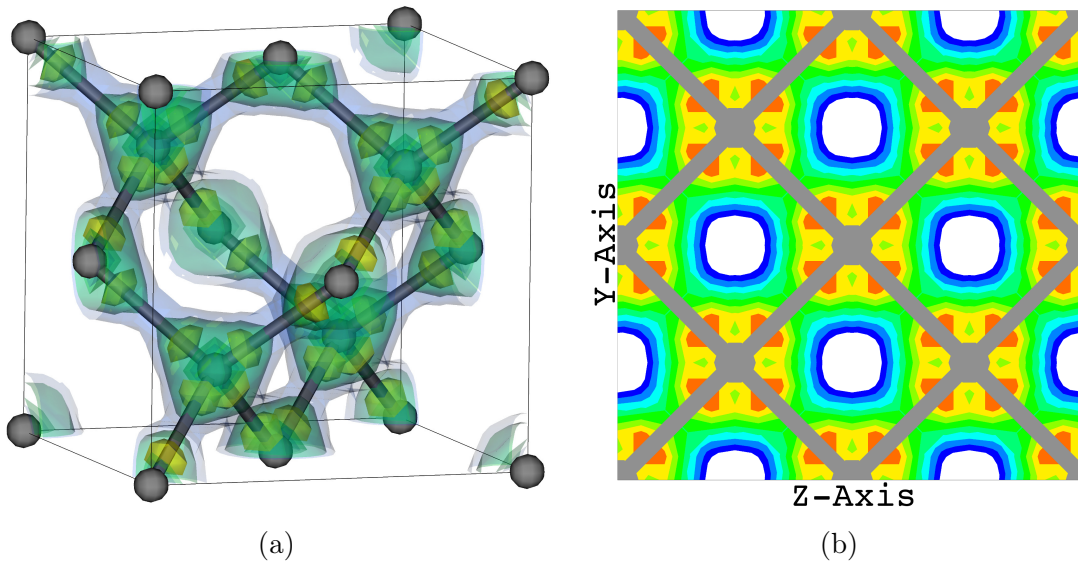


Figure 2.4: Ground state electron density of diamond. (a) 3-dimensional. (b) Projection onto the yz-plane (z is the laser pulse polarization direction).

four valence electrons ($2s^2 2p^2$) of each C atom form new $2(sp^3)$ hybrid orbitals with equal energy when placed in the diamond structure. The resulting covalent bonds show largely overlapping orbitals and are therefore very strong. This is the reason for diamond being so hard.

2.1.2 Linear response

The response to optical excitation of diamond was studied by applying a weak delta-shaped field impulse to the material.

The dielectric function can be derived from the induced microscopic current density $\mathbf{j}(\mathbf{r}, t)$ defined as

$$\mathbf{j}(\mathbf{r}, t) = \sum_i \frac{1}{2} \left[\psi_i^*(\mathbf{r}, t) \left(-i\nabla + \frac{1}{c} \mathbf{A}(t) \right) \psi_i(\mathbf{r}, t) + \text{c.c.} \right] \quad (2.2)$$

and evaluated at every time step. The macroscopic current density $\mathbf{J}(t)$ within the whole unit cell is then given by the average over the unit cell volume Ω ,

$$\mathbf{J}(t) = \frac{1}{\Omega} \int_{\Omega} d\mathbf{r} \mathbf{j}(\mathbf{r}, t). \quad (2.3)$$

In order to compute the dielectric function along the laser polarization direction only the component of the macroscopic current density $\mathbf{J}(t)$ along this direction is required,

$$J(t) = \mathbf{J}(t) \cdot \mathbf{F}_0 / |\mathbf{F}_0|. \quad (2.4)$$

According to Ohm's law, the frequency dependent conductivity $\sigma(\omega)$ is given by the ratio of the Fourier transforms of the macroscopic current density and the

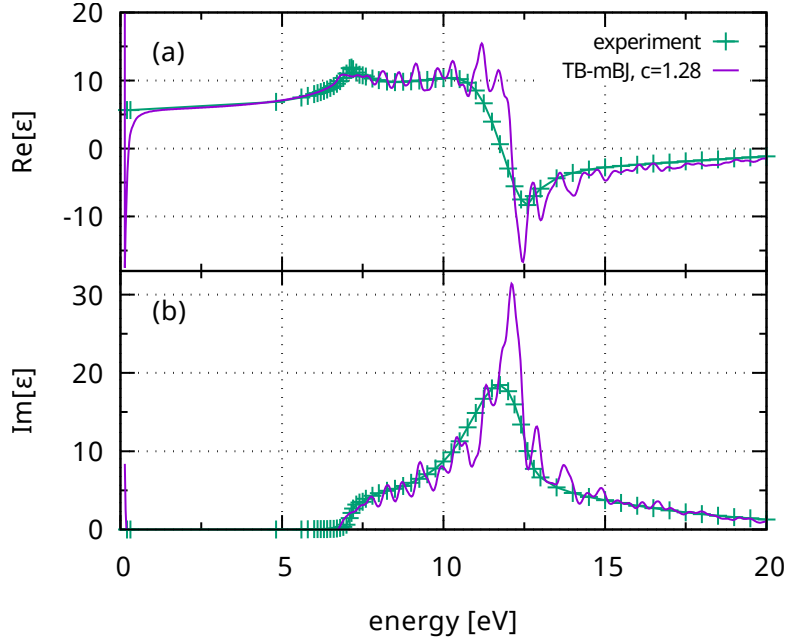


Figure 2.5: Real (a) and imaginary (b) part of the dielectric function of diamond. Purple: calculated; green: experiment [25].

electric field,

$$\sigma(\omega) = \frac{\int_{-\infty}^{\infty} dt e^{i\omega t} J(t)}{\int_{-\infty}^{\infty} dt e^{i\omega t} F(t)}. \quad (2.5)$$

Finally, the dielectric function $\epsilon(\omega)$ follows from its direct relationship to the conductivity $\sigma(\omega)$,

$$\epsilon(\omega) = 1 + \frac{4\pi i \sigma(\omega)}{\omega}. \quad (2.6)$$

The calculated real and imaginary parts of the dielectric function of diamond are presented in Fig. 2.5 (purple line) along with experimental results (green crosses and lines). The overall agreement is good for energies larger than 1 eV. Also the excitation gap matches the experimental value. Towards very small energies, both the real and imaginary parts show a singularity. This is probably related to the discretization of the real space that reduces the translational symmetry as

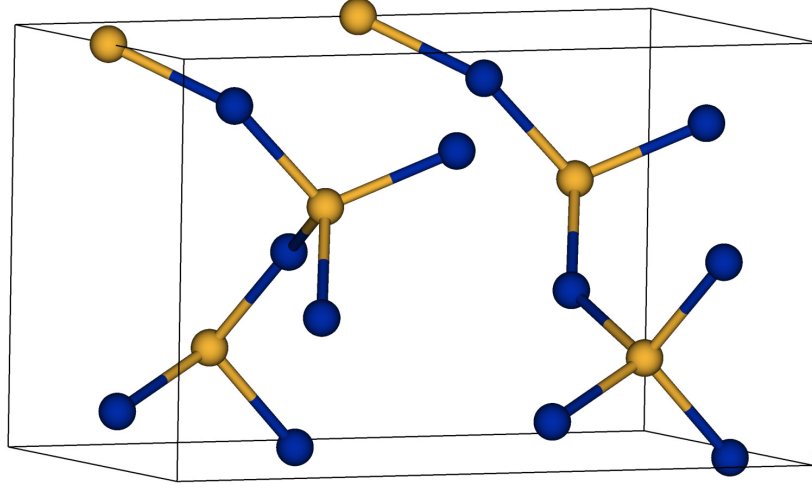


Figure 2.6: Unit cell of SiO_2 as used in the calculations. The silicon atoms are shown yellow whereas the oxygen atoms are blue.

compared to the continuous space [26]. This effect may lead to a small constant offset in the current density of time-dependent calculations.

2.2 α -Quartz (SiO_2)

Similarly, SiO_2 in the form of α -quartz was studied. This material crystallizes in the trigonal crystal system and belongs to the $P3_121$ space group. α -quartz shows both a threefold and a twofold rotational symmetry. However, none of the appearing symmetries can be utilized in the simulations due to the polarization direction of the laser pulse which breaks those rotational symmetries.

In α -quartz each Si atom is surrounded by 4 O atoms in a tetrahedron. The corner O atoms are shared between two adjacent tetrahedra. The cuboid unit cell used in the simulations is shown in Fig. 2.6. It contains a total of 18 atoms, 6 Si atoms and 12 O atoms, with a volume of $4.91 \text{ \AA} \times 8.51 \text{ \AA} \times 5.41 \text{ \AA}$ [27]. Each of the 6 SiO_2 units has 16 valence electrons. In total, the unit cell contains 96

electrons with 52 bands taken into account. $20 \times 36 \times 50$ spatial grid points are used whereas at least $4 \times 4 \times 4$ reciprocal grid points are needed. These settings turned out to be the best compromise between numerical cost and accuracy for the TDDFT calculations.

2.2.1 Ground state properties

Employing the TB-mBJ XC potential allows for an accurate reproduction of the band gap in SiO_2 . The prescription by Tran and Blaha [8] to set $c = 1.00$ for the TB-mBJ functional was followed. The calculated excitation gap energy was $\Delta_{TB-mBJ} = 7.78 \text{ eV}$ and is in reasonable agreement with experimental values [28] ($\Delta_{exp} = 8.9 \text{ eV}$) and other calculations [29, 30] ($\Delta_{calc} = 9.2 \text{ eV}$ and 6.3 eV respectively). The calculated band gap value was extracted from the energy eigenvalues of the Kohn-Sham orbitals $\psi_j(\mathbf{r}, t)$. A different method to obtain the excitation gap energy is to take the optical energy at which the imaginary part of the dielectric function becomes larger than zero. This value (see subsection 2.2.2) was $\Delta_\varepsilon = 8.9 \text{ eV}$, supporting the choice of $c = 1.00$.

The $4 \times 4 \times 4$ \mathbf{k} -grid was the coarsest grid to allow for convergence for most of the observables. Using 4 computational nodes with a total of 64 cores convergence of the ground state was reached after about 150 iterations of minimization within less than 10 min. Fig. 2.7 shows the convergence process for SiO_2 . Convergence of both the energy and the electron density was slower than for diamond and was accomplished after about 130 iterations. The final ground state energy was $E_{GS} = -5890.4 \text{ eV}$.

Furthermore, the occupied and unoccupied densities of states are illustrated in

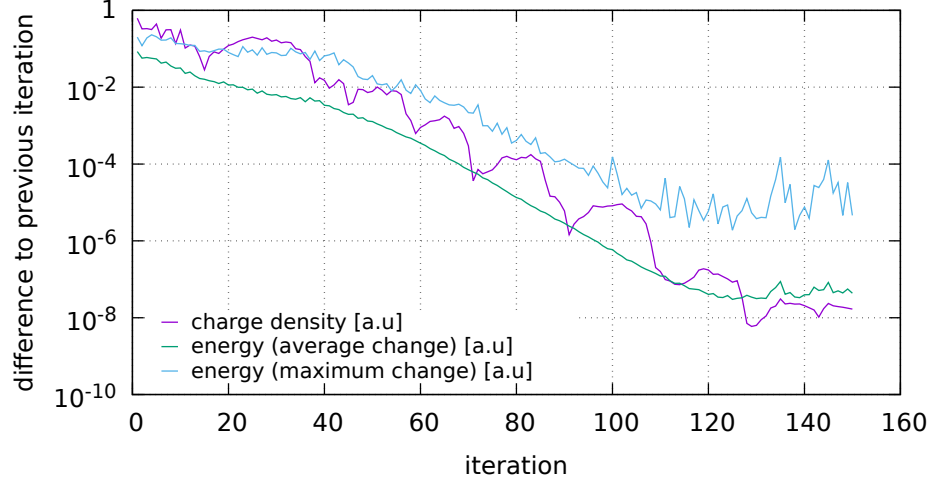


Figure 2.7: Ground state convergence process for SiO_2 showing the per-iteration change of the charge density as well as the average and the maximum change of the energy per \mathbf{k} -point.

Fig. 2.8. For energies close to the Fermi energy the agreement with the experiment in [29, 30] is good, yet shifts of about 3 eV, 2 eV, and 1 eV appear in the calculations for the three bands below the Fermi energy. This is a consequence of using the TB-mBJ XC potential which increases the band gap energy at the cost of spreading out the whole band structure leaving only the Fermi energy unchanged.

The density of states of SiO_2 can be split into several regions:

- Deeply bound O ($2s$) states from -19 to -16 eV (experimental maximum near -21 eV).
- Si s states around -8 eV (experimental maximum near -11 eV).
- p states of O and Si around -6 eV (experimental maximum near -8 eV).
- The top of the valence band is formed predominantly by non-bonding p -like O orbitals around -2 eV (experimental maximum near -3 eV).

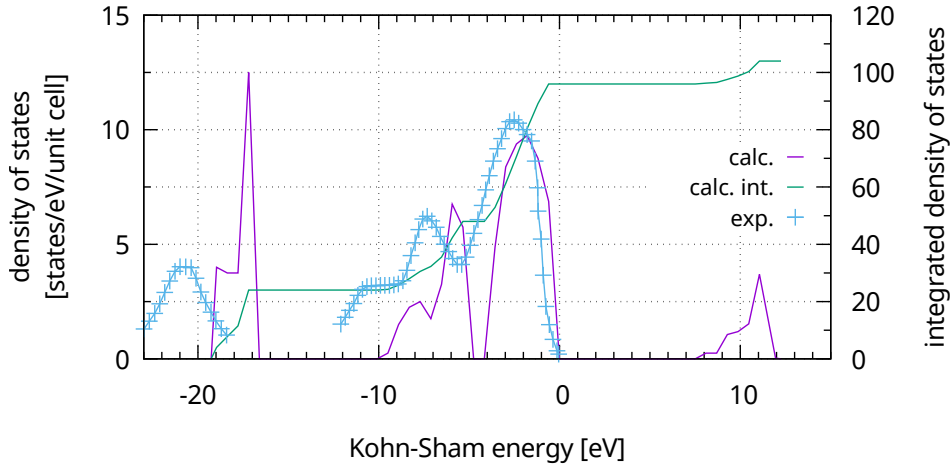


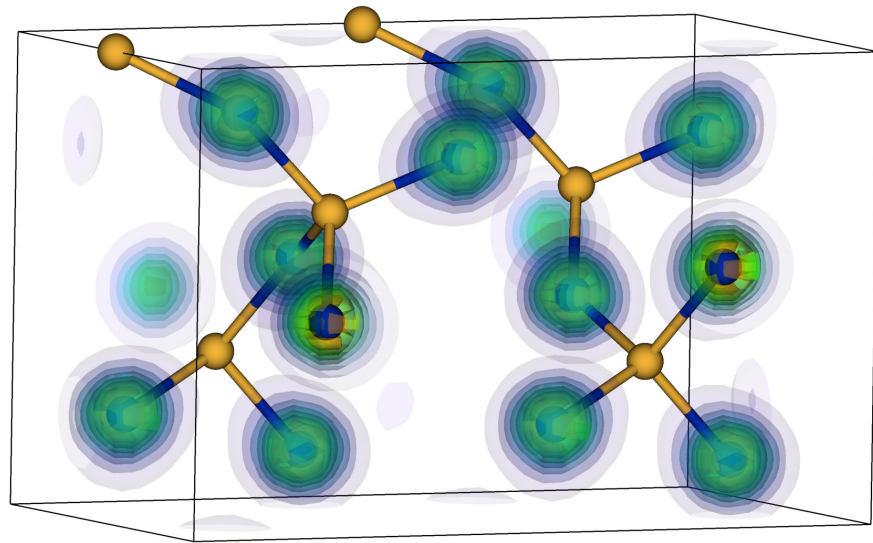
Figure 2.8: Ground state density of states (calculated and occupied experimental [29]) and integrated density of states for SiO_2 . The zero-point on the energy scale is defined as the top of the valence band.

- The lowest conduction band levels appear at around 8 eV.

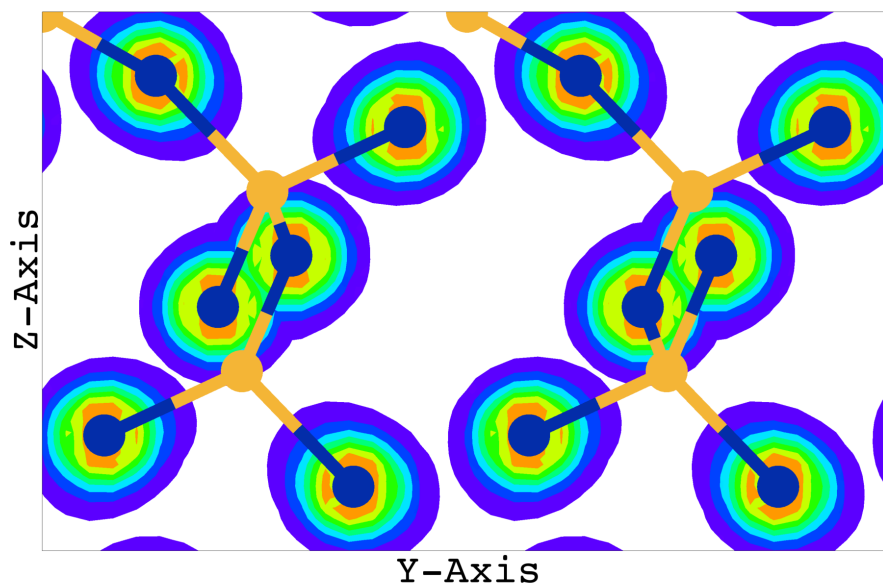
The ground state electron density is shown in Fig. 2.9 and reveals that the highest density inside the unit cell is located around the oxygen atoms due to the larger number of electronic orbitals contained in the simulation (6 vs. 4 for Si) and the high electron affinity of oxygen attracting charge from the Si core towards the O core.

2.2.2 Linear response

As described in subsection 2.1.2 the dielectric function for SiO_2 was calculated and compared to experimental data (Fig. 2.10). The agreement of the calculated and the experimental values is reasonable. The band gap is correctly reproduced but equally to diamond a singularity at very low energies appears.



(a)



(b)

Figure 2.9: Ground state electron density of SiO_2 . (a) 3-dimensional. (b) Projection onto the yz -plane. The charge is located almost symmetrically around the oxygen atoms with slight deformations towards the silicon atoms.

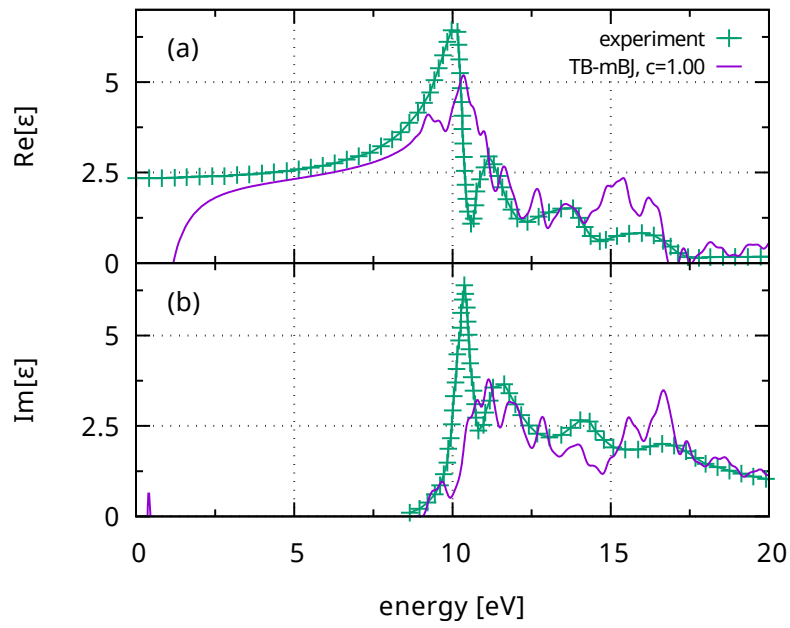


Figure 2.10: Real (a) and imaginary (b) parts of the dielectric function of SiO_2 . Purple: calculated; green: experiment [31].

3 Single crystal unit cells

Due to the periodicity of the crystal lattice the study of electron dynamics within solids can be spatially limited to the smallest unit of periodicity. Propagation effects, e.g. surface polarization or polarization along the laser propagation direction, are neglected in the simulations of single crystal unit cells. All calculations were performed on the Vienna Scientific Cluster. The TDDFT time step was set to $\Delta t = 0.02 \text{ a.u.} \approx 0.5 \text{ as}$ for all the single cell calculations. For a typical total pulse duration used in the simulations of $\tau_p = 20 \text{ fs}$ the calculation time for the time evolution of the system was approximately 4 h 45 min on 5 computational nodes.

3.1 Single color laser pulses

In order to investigate the primary effects of ultra-short high-intensity laser pulses on bulk solids a time-dependent laser field determined by the vector potential

$$\mathbf{A}(t) = \begin{cases} \frac{\mathbf{F}_0}{\omega} \sin^2\left(\frac{\pi}{\tau_p}t\right) \cos\left(\omega t - \omega \frac{\tau_p}{2} + \phi_{CE}\right), & \text{if } 0 < t < \tau_p \\ \mathbf{0}, & \text{otherwise} \end{cases} \quad (3.1)$$

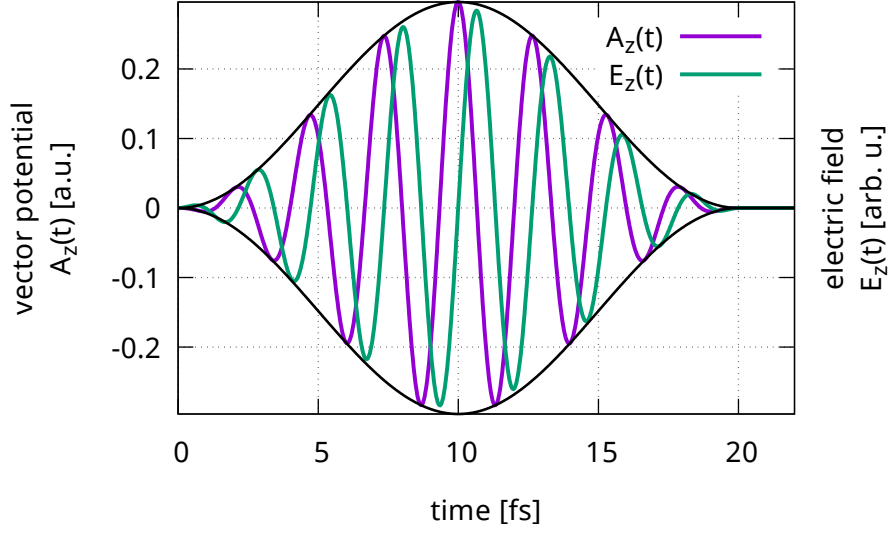


Figure 3.1: Time-dependent vector potential and electric field of a 800 nm laser pulse for medium intensity ($1 \times 10^{13} \text{ W/cm}^2$) and $\phi_{CE} = 0$.

was applied. This vector potential employs a \sin^2 envelope where \mathbf{F}_0 indicates the amplitude and the polarization direction, ω is the laser carrier frequency, τ_p the total pulse duration (FWHM of the field is $\tau_p/2$), and ϕ_{CE} the carrier-envelope phase. For $\phi_{CE} = 0$ the maximum of the potential coincides with the maximum of the envelope function at $\tau_p/2$ in positive field direction (Fig. 3.1).

In this thesis the interaction of single color laser pulses with diamond was investigated, following similar studies performed earlier by Wachter et al. for SiO_2 [32]. Another reason for the choice of diamond is the low computational cost due to the high symmetry of the crystal structure allowing for a large number of parameters to be varied in this study. Wachter et al. have shown that a finite amount of charge is transferred by nonlinear polarization currents during the laser pulse which can be associated with a field-induced conductivity. This can be viewed as a reversible (sub)femtosecond-scale insulator to metal transition where the conductivity in-

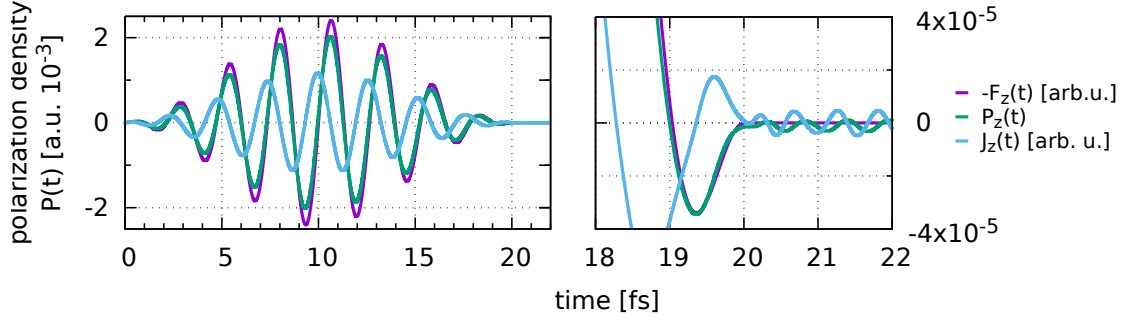


Figure 3.2: Polarization density, macroscopic current density and laser field for a 20 fs laser pulse with carrier envelope phase $\phi_{CE} = \pi$ and intensity $1 \times 10^{12} \text{ W/cm}^2$.

creases by more than 20 orders of magnitude on a femtosecond timescale. The amount of charge transferred by the laser pulse is found to be strongly dependent on the laser intensity, the pulse shape (especially the carrier-envelope phase ϕ_{CE}) and the laser polarization direction.

To calculate the polarization $\mathbf{P}(t)$ of the unit cell the macroscopic current density (Equation 2.3) is integrated,

$$\mathbf{P}(t) = \int_0^t dt' \mathbf{J}(t'), \quad (3.2)$$

where $t' = 0$ indicates the start of the simulation. Figure 3.2 shows the macroscopic current density and the polarization along the laser polarization direction for a laser pulse with an intensity of $1 \times 10^{12} \text{ W/cm}^2$ and $\phi_{CE} = 0.5\pi$. The current density follows the laser field with a phase shift of $\pi/2$ while the polarization density is in phase with the field except for a sign flip due to the negative charge of the electrons. After the conclusion of the pulse the current density goes back to zero while the polarization density becomes very small but stays finite due to non-linear

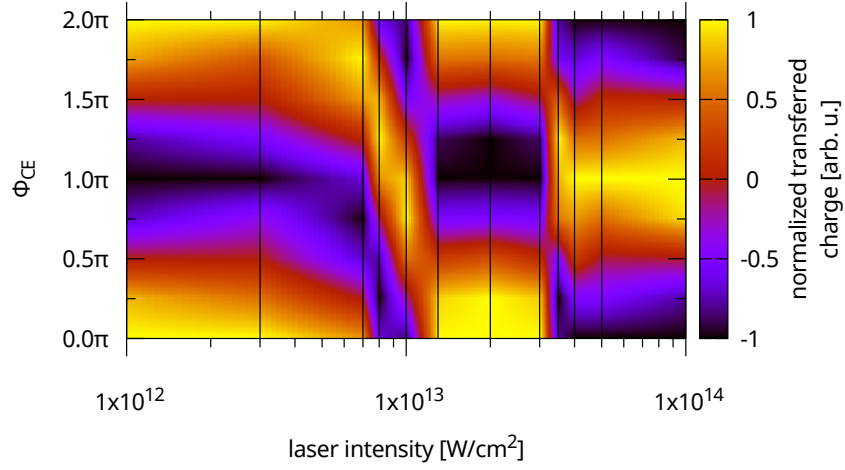


Figure 3.3: Intensity and carrier-envelope phase dependence of the transferred charge normalized to the maximum charge transferred in positive or negative direction along the polarization axis. Vertical black lines indicate calculated values, in between the values are interpolated bilinearly. A phase shift as a function of the intensity is observed between $I_c^{(1)} \approx 5 \times 10^{12} \text{ W/cm}^2$ and $I_c^{(2)} \approx 5 \times 10^{13} \text{ W/cm}^2$.

polarization currents induced during the pulse.

The total macroscopic charge transferred along the laser polarization axis is given by

$$Q = \mathcal{A}_{\text{eff}} \frac{\mathbf{F}_0/|F_0|}{\Delta t} \int_{\tau_p}^{\tau_p + \Delta t} dt' \mathbf{P}(t'), \quad (3.3)$$

where the polarization is averaged over a time span $\Delta t = 8 \text{ fs}$ after the conclusion of the pulse before major damping effects would set in. The factor \mathcal{A}_{eff} has to be obtained by comparison with experiments and is a measure of the effective charge collecting surface area orthogonal to the polarization direction.

Due to the crystal symmetry of diamond laser pulses with $\phi_{CE} = (n + 1/2)\pi$, $n \in \mathbb{Z}$ do not result in an effective charge transfer in the linear regime, as can be seen in Fig. 3.3. Asymmetric pulses with the peak vector potential pointing in positive or negative laser polarization direction ($\phi_{CE} = n\pi$, $n \in \mathbb{Z}$) result in

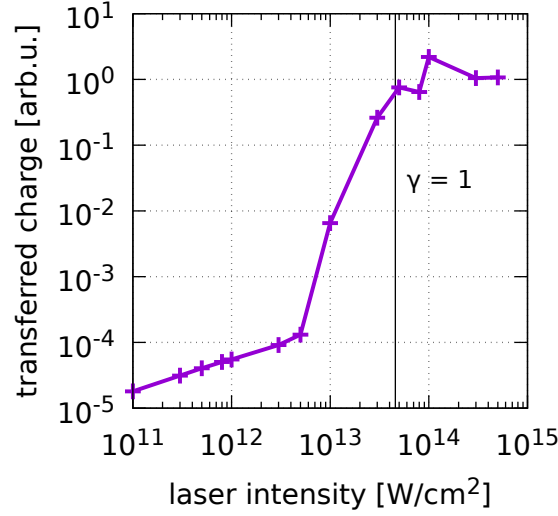


Figure 3.4: Total transferred charge within the diamond unit cell as function of the laser intensity for wavelength $\lambda = 800$ nm ($\omega \approx 1.55$ eV), pulse length $\tau_p = 20$ fs and carrier envelope phase $\phi_{CE} = \pi$.

charge transfer. As expected, the transferred charge follows a cosine curve in the linear regime, but only for very short laser pulses, $\tau_p \lesssim 15$ fs (compare [33, 34]). For longer laser pulse durations, with a rising number of laser cycles $n = \tau_p \omega / (2\pi)$ underneath the envelope, the influence of ϕ_{CE} gradually decreases as observed for many time-dependent phenomena.

At an intensity of about $I_c^{(1)} \approx 5 \times 10^{12}$ W/cm² the transition from the linear to the non-linear regime is observed. A strong non-linear increase of Q is predicted (Fig. 3.4) together with a phase shift increasing as a function of the laser intensity. Above $I_c^{(2)} \approx 5 \times 10^{13}$ W/cm² the phase dependence of Q stabilizes again at a phase shift of $\Delta\phi_{CE} = \pi$ with respect to the linear regime and with 4 orders of magnitude more charge transferred (Fig. 3.3 and 3.4) in good agreement with previous investigations [35].

The onset of non-linearities also becomes visible when looking at other observ-

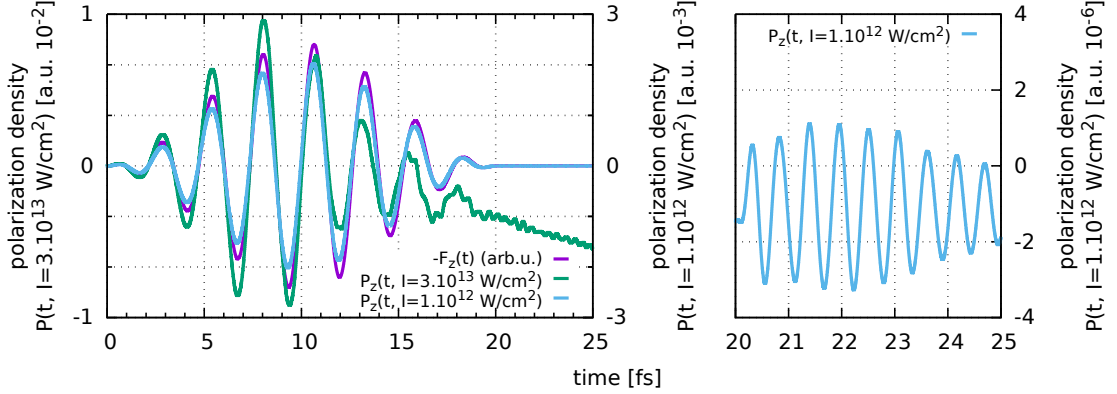


Figure 3.5: Comparison of polarization densities for two intensities: below ($I = 1 \times 10^{12} \text{ W/cm}^2$) and around ($I = 3 \times 10^{13} \text{ W/cm}^2$) the non-linearity threshold including a zoom into the polarization density of the weaker laser pulse after the pulse conclusion.

ables, e.g., the polarization density within the unit cell. In Fig. 3.5 $P_z(t)$ is shown for an intensity in the linear regime ($I = 10^{12} \text{ W/cm}^2$, light blue line) and an intensity in the non-linear regime ($I = 3 \times 10^{13} \text{ W/cm}^2$, green line) together with the electric field (purple line). While $P_z(t)$ closely follows $-F_z(t)$ over the whole propagation time, strong non-linearities appear around the maximum of the pulse, leading to polarization remaining in the system even after conclusion of the pulse. This is equivalent to a constant current flowing in the system as it was observed for SiO_2 excited by strong laser pulses [32]. This current can be associated with a field-induced conductivity $\sigma(\omega)$ and leads to a reversible transition of the insulator to a metal on the fs-timescale. So far, dissipative processes such as electron-phonon or electron-electron scattering are not yet accounted for in our simulations but would lead to a quick reduction $\sigma(\omega)$ after the conclusion of the pulse instead of the remaining oscillating offset in the zoomed part of Fig. 3.5.

The situation changes again when the laser intensity or, equivalently, the peak electric field reaches the tunnel regime. In this regime valence band electrons may

tunnel through the band gap to the strongly deformed conduction band (horizontal transition). Excited electrons create a macroscopic current flowing even after the laser pulse. As explained before, for a Keldysh parameter of $\gamma \gg 1$ multi-photon excitation dominates while $\gamma \ll 1$ indicates tunnel ionization. For diamond with a band gap of about $\Delta \approx 5.5$ eV and a laser energy of $\hbar\omega = 1.55$ eV the intensity to reach $\gamma = 1$ is $I = 4.57 \times 10^{13}$ W/cm². Even higher intensities result in an optical breakdown of the material.

To depict the impact of a strong laser pulse ($I = 3 \times 10^{13}$ W/cm², $\tau_p = 20$ fs) on the charge distribution Fig. 3.6 and Fig. 3.7 show the induced charge density

$$\delta n(\mathbf{r}, t) = n(\mathbf{r}, t) - n_0(\mathbf{r}) \quad (3.4)$$

for two different times. In Fig. 3.6 the induced charge density at the maximum electric field peak ($t = 10$ fs) is shown. The density is displaced along the laser polarization direction. After the conclusion of the pulse (Fig. 3.7) the density does not return to its ground-state distribution. Delocalized conduction band states in the interstitial regions of the carbon atoms are populated, leading to an increased electron density between adjacent atoms.

3.2 Two-color laser pulses

So far, the left/right asymmetry of the transferred charge was induced into the system by modulation of the carrier-envelope phase of ultra-short laser pulses. However, this is difficult to achieve and to control experimentally. For longer pulses ($\tau_p \gtrsim 15$ fs) carrier-envelope phase effects disappear.

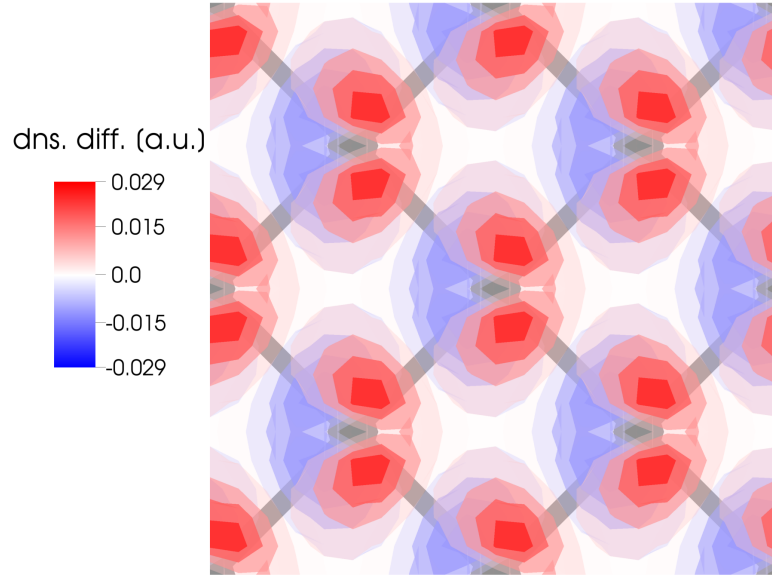


Figure 3.6: Projection of the induced charge density onto the yz-plane for a strong pulse ($I = 3 \times 10^{13} \text{ W/cm}^2$, $\tau_p = 20 \text{ fs}$) at $t = 10 \text{ fs}$ (positive maximum of electric field). The laser polarization direction is from left to right (z-axis).

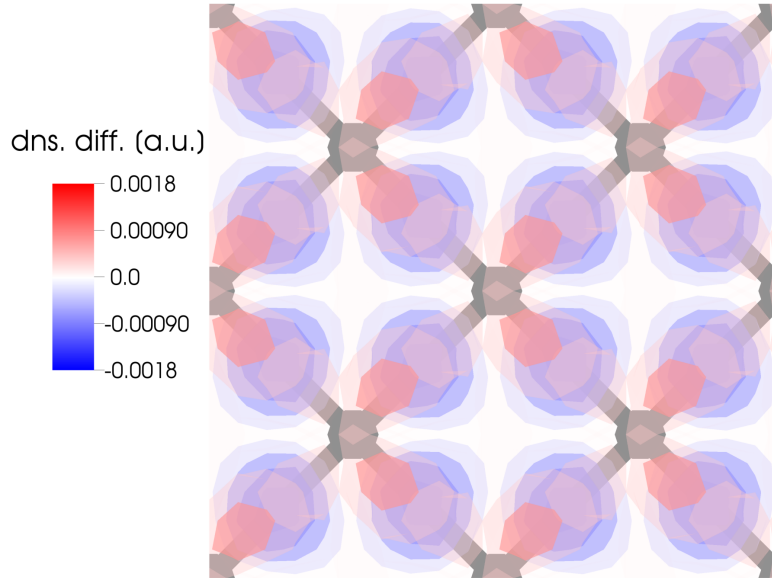


Figure 3.7: Projection of the induced charge density onto the yz-plane for a strong pulse ($I = 3 \times 10^{13} \text{ W/cm}^2$, $\tau_p = 20 \text{ fs}$) 4 fs after the conclusion of the laser pulse. The laser polarization direction is from left to right (z-axis). The color scale is more than one order of magnitude smaller compared to Fig. 3.6.

Alternatively, asymmetries of the field can be induced by adding a second, superimposed laser pulse with controlled relative phase locked to the phase of the primary pulse. This is usually achieved by generating the secondary pulse using part of the primary pulse and selectively shifting the relative phase by insertion of fused silica wedges. Equations 3.5 describe both vector potentials of the laser pulses.

$$\mathbf{A}_1(t) = \frac{\mathbf{F}_{01}}{\omega_1} \sin^2 \left(\frac{\pi}{\tau_{p1}} t \right) \cos \left(\omega_1 t - \omega_1 \frac{\tau_{p1}}{2} + \phi_{CE1} \right), \quad \text{if } 0 < t < \tau_{p1}. \quad (3.5a)$$

$$\mathbf{A}_2(t) = \frac{\mathbf{F}_{02}}{\omega_2} \sin^2 \left(\frac{\pi}{\tau_{p2}} t \right) \cos \left(\omega_2 t - \omega_2 \frac{\tau_{p2}}{2} + \phi_{CE2} \right), \quad \text{if } \tau_{12} < t < \tau_{12} + \tau_{p2}. \quad (3.5b)$$

In general, the amplitudes \mathbf{F}_{0j} , the pulse lengths τ_{pj} , the carrier frequencies ω_j and the carrier-envelope phases ϕ_{CEj} can be different for both laser pulses. A possible time shift between the two pulses is not considered by setting $\tau_{12} = 0$ fs. Furthermore, the analysis was restricted to pulses of equal duration, $\tau_{p1} = \tau_{p2} = \tau_p$, and frequency doubled secondary pulses, $\omega_2 = 2\omega_1$. The 2ω laser pulse is only a small perturbation to break the symmetry of the electric field. Hence, the amplitude \mathbf{F}_{02} was chosen to have the same polarization direction and a small fraction of the first pulse's field strength, $\mathbf{F}_{02} = \xi \mathbf{F}_{01}$ with $\xi \ll 1$. As for longer laser pulses, the carrier-envelope phase does not have any influence on the asymmetry of the results. Only the relative phase $\Delta\phi$, defined by

$$\phi_{CE1} = \phi_{CE}, \quad (3.6a)$$

$$\phi_{CE2} = 2\phi_{CE} + \Delta\phi, \quad (3.6b)$$

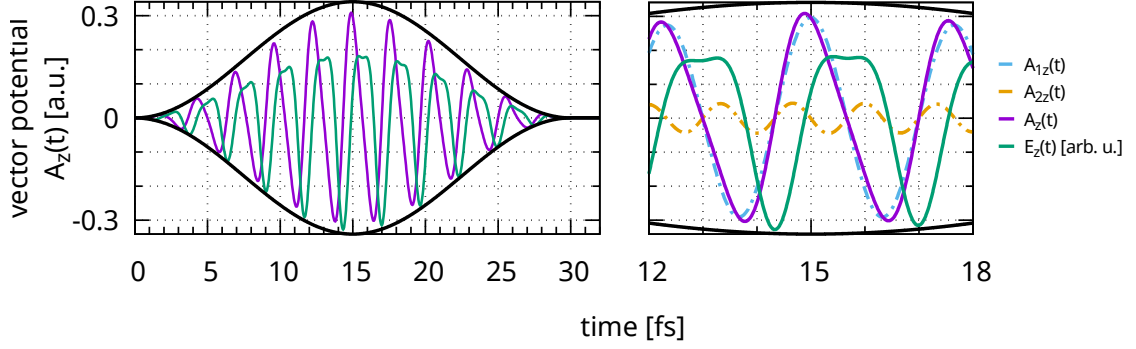


Figure 3.8: Time-dependent vector potential and electric field of two superimposed 800 nm and 400 nm laser pulses ($\tau_p = 30$ fs) for medium intensity (1×10^{13} W/cm²), carrier-envelope phases $\phi_{CE1} = 0$ and $\phi_{CE2} = \pi/2$, and mixing ratio $\xi = 0.3$.

is important. The carrier-envelope phase ϕ_{CE} shifts both pulses equally in time with respect to the envelope function whereas the two-color phase $\Delta\phi$ only shifts the second, weaker pulse against the first, stronger one.

With these restrictions 6 free parameters, \mathbf{F}_{01} , ξ , ω_1 , τ_p , and the phases ϕ_{CE} and $\Delta\phi$ remain to be varied. The total vector potential is given by the sum of the two individual pulses,

$$\mathbf{A}(t) = \mathbf{A}_1(t) + \mathbf{A}_2(t). \quad (3.7)$$

Figure 3.8 shows the vector potential of a two-color laser pulse and its two components together with the electric field. With $\phi_{CE} = \Delta\phi = 0$ and mixing ratio $\xi = 0.3$ the resulting vector potential and the electric field are asymmetric despite the long pulse duration.

To observe the asymmetric charge transfer introduced by the two-color field first its dependence on the phases ϕ_{CE} and $\Delta\phi$ is investigated. The primary field strength is in the non-linear regime ($I_1 = 5 \times 10^{13}$ W/cm²) while the second color's intensity ($\xi = 0.2$, $I_2 = 2 \times 10^{12}$ W/cm²) lies in the linear regime.

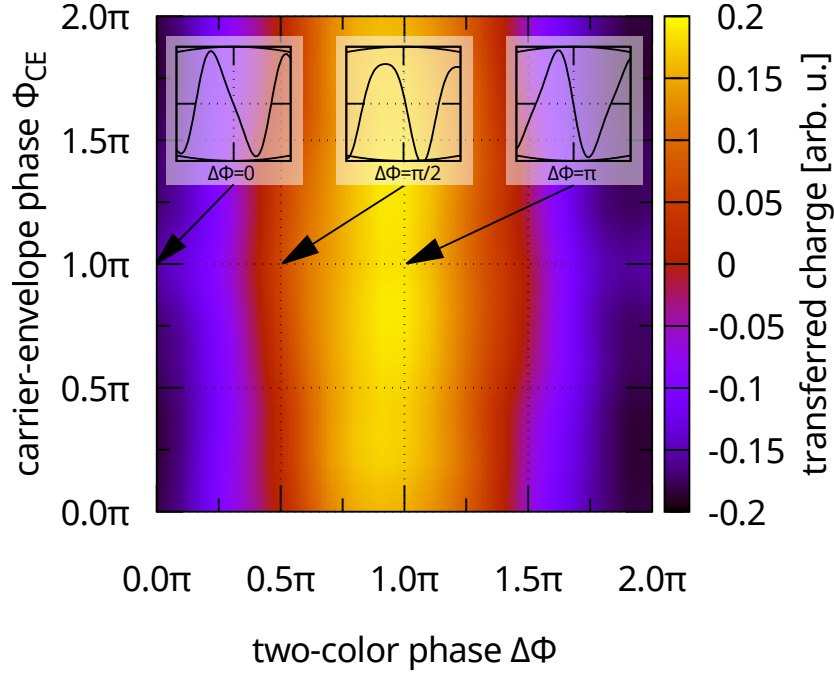


Figure 3.9: Transferred charge dependence on the carrier-envelope ϕ_{CE} and two-color phase $\Delta\phi$ for primary laser pulse intensity $I_1 = 5 \times 10^{13} \text{ W/cm}^2$, mixing ratio $\xi = 0.2$, and pulse length $\tau_p = 20 \text{ fs}$. The two-color phase variation is about one order of magnitude larger than the carrier-envelope phase variation. The insets show the electric field of the laser pulse near the maximum amplitude for 3 different two-color phases $\Delta\phi \in \{0, \pi/2, \pi\}$.

Figure 3.9 shows the transferred charge as a function of ϕ_{CE} and $\Delta\phi$. Due to the long pulse length of $\tau_p = 20 \text{ fs}$ an almost vanishing variation with ϕ_{CE} is found. On the other hand, variation of the two-color phase induces a sinusoidal variation of the charge transferred to the positive or the negative laser polarization direction.

For a primary intensity below $I_c^{(1)}$, adding a weak two-color field may drive the system into the non-linear regime, $I_1 + I_2 > I_c^{(1)}$. Therefore, an even stronger dependence of the transferred charge on the relative phase $\Delta\phi$ is expected. First calculations for a primary laser intensity of $I_1 = 5 \times 10^{12} \text{ W/cm}^2$ and secondary intensity $I_2 = 5 \times 10^{11} \text{ W/cm}^2$ ($\xi = \sqrt{0.1}$) showed that the kink appearing around

$5 \times 10^{12} \text{ W/cm}^2$ in Fig. 3.4 needs to be resolved better in order to tune the intensities of the two pulses in such that the total intensity varies around the kink.

3.3 Semiclassical estimate

As described in section 1.4 semiclassical simulations were performed for diamond. The parameters extracted from the TDDFT calculations are: $\Delta V = 5 \text{ eV}$, $\lambda_{ion} = 178.33 \text{ pm}$ and $\Delta = 5.46 \text{ eV}$. ΔV is estimated with an upper boundary of the band gap Δ and λ_{ion} is the periodic distance of carbon atoms along the z -direction which is the laser polarization direction. Figure 3.10 shows the trajectories of 6 electrons simulated with a laser intensity of $I = 5 \times 10^{13} \text{ W/cm}^2$ in the tunnel ionization regime.

For this parameter set the carrier-envelope and two-color phase dependent charge asymmetry is shown in Fig. 3.11a. For every combination of carrier-envelope phase ϕ_{CE} and two-color phase $\Delta\phi$ a total of 5000 electron trajectories were simulated. The magnitude of the introduced ionic potential is responsible for the visible artefacts and fluctuations when compared to Fig. 3.9. Setting $\Delta V = 0 \text{ eV}$ and thus simulating quasi free electrons in the conduction band the results turn out to be in better agreement with the TDDFT calculations (Fig. 3.11b). This indicates that the strong-field approximation is applicable in the case of laser-solid interactions. All further simulations were therefore executed without ionic potential.

Another characteristic that can be reproduced by the semiclassical model is the phase shift of the carrier-envelope dependence on the laser intensity (see Fig. 3.3). The intensity dependence of the phase shift is calculated with both the ADK rate and the multi-photon ionization rate. The results are shown in Fig. 3.13.

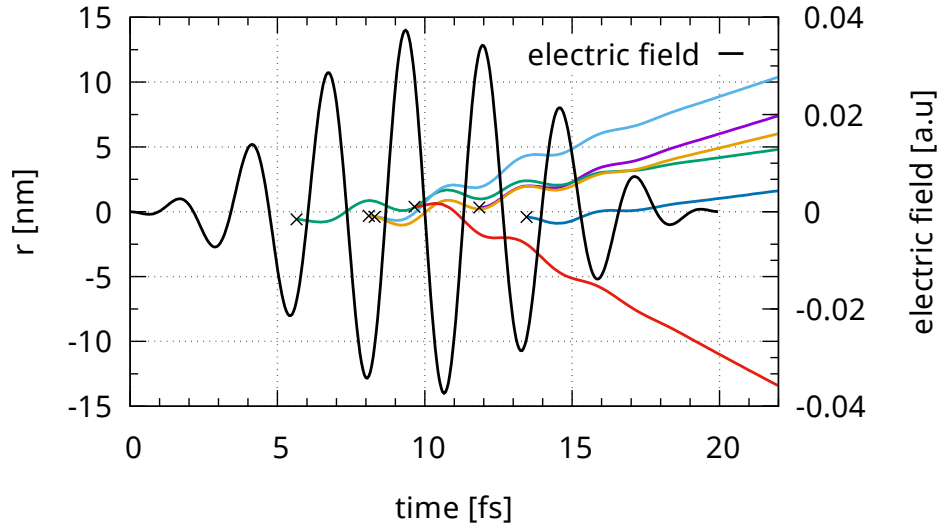


Figure 3.10: Electron trajectories in a laser field and a crystal potential. The colored lines show the trajectories, the black line indicates the laser field strength. The black crosses illustrate the ionization times and positions.

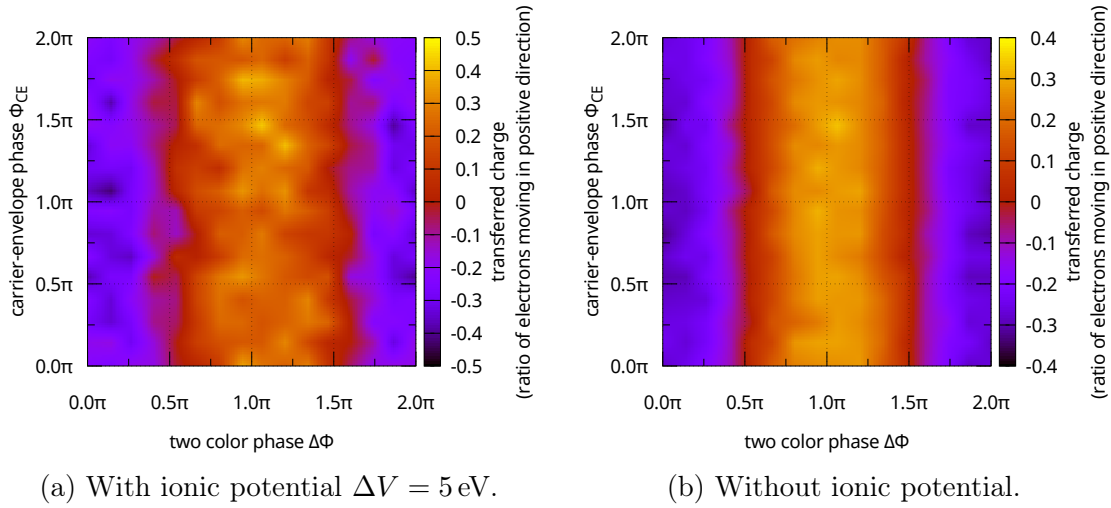


Figure 3.11: Semiclassically calculated transferred charge dependence on the carrier-envelope phase ϕ_{CE} and two-color phase $\Delta\phi$ for primary laser pulse intensity $I_1 = 5 \times 10^{13}$ W/cm², mixing ratio $\xi = 0.2$, and pulse length $\tau_p = 20$ fs.

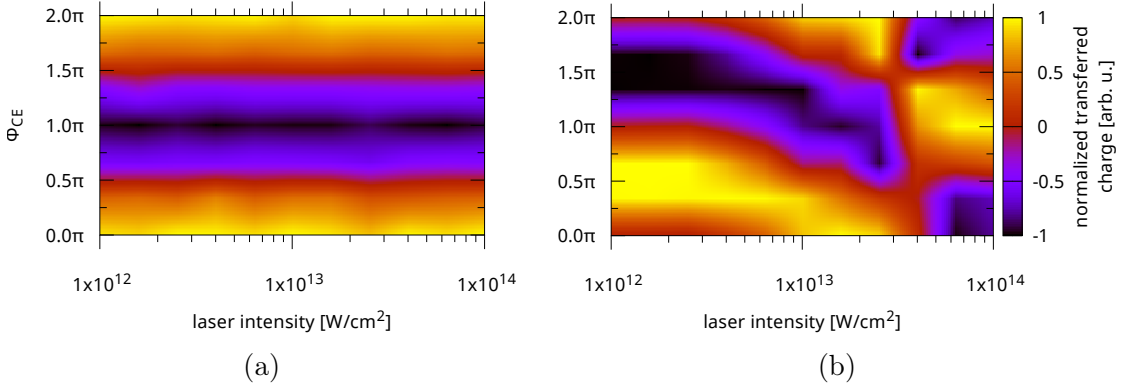


Figure 3.12: Intensity and carrier-envelope phase dependence of the transferred charge normalized to the maximum charge transferred in positive or negative direction along the polarization axis for employing the multi-photon ionization rate (a) and the ADK ionization rate (b).

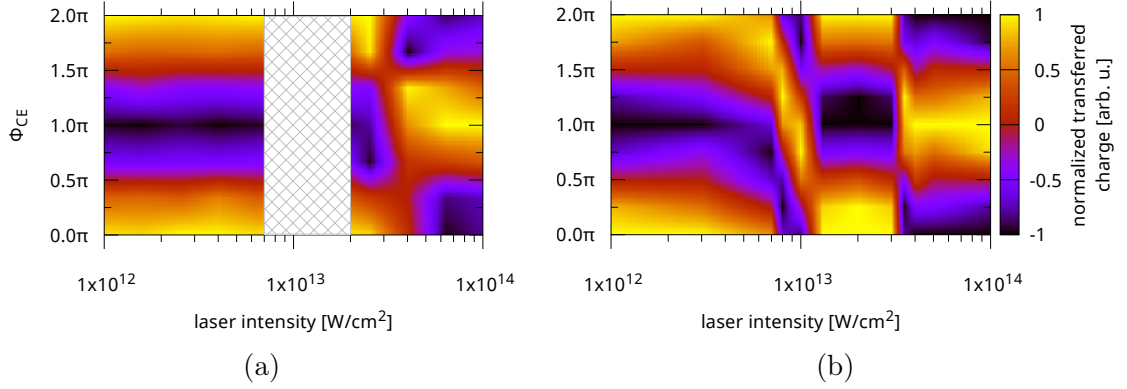


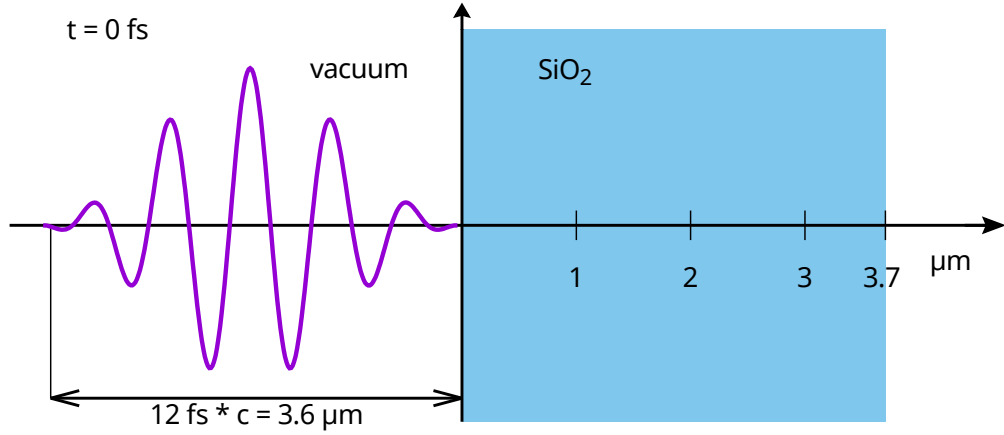
Figure 3.13: (a) Phase dependence of multi-photon (left) and tunneling ionization (right) for $\gamma \gg 1$ and $\gamma \ll 1$. Dominant features of the TDDFT simulation (b) are well reproduced by the semiclassical estimate.

Both models agree with the TDDFT calculation in the weak and strong field regimes ($\gamma = 1$ for $I = 4.57 \times 10^{13} \text{ W/cm}^2$) as can be seen in Fig. 3.13. Only the intensity range from $7 \times 10^{12} \text{ W/cm}^2$ to $2 \times 10^{13} \text{ W/cm}^2$ where both processes contribute to the total ionization cannot be modelled with this simple simulation. Therefore computationally demanding TDDFT calculations can be restricted to this transition regime rendering the semiclassical model an important tool to study the phase dependence of charge transfer in dielectrics at low computational cost.

4 Multiscale coupled dynamics

The physical description in the previous sections holds true only in the case of perfectly flawless, infinitely extended crystals in which laser pulses can propagate freely and do not couple to the electron dynamics induced inside the unit cells. Real crystals, however, show surface effects caused by the phase transition from vacuum to the insulator. Furthermore, the laser pulse experiences a chirp caused by chromatic dispersion or non-linearities and the induced currents couple to the electric field.

In order to account for these effects and investigate their impact on the charge transfer, multiscale simulations were performed. Since at each macroscopic grid point a full single cell calculation has to be completed, the computational effort is significantly higher for multiscale simulations. The required computational resources were provided on the K computer, a supercomputer located at Kobe, Japan, with approximately 20 times more cores than the local Vienna Scientific Cluster. To illustrate the differences in computational workload between single cell and multiscale simulations the total number of cores used and the runtime can be compared. A typical microscopic TDDFT calculation for SiO_2 takes 17.5 h on 64 cores (corresponding to 4 nodes) on the Vienna Scientific Cluster. Applying the same parameters in a multiscale calculation that employs 280 macroscopic grid

Figure 4.1: Laser pulse at $t = 0$ fs.

points (with a spacing of 13.2 nm and a total material thickness of 3.7 μm) and performing it on 71680 cores (corresponding to 8960 of the approximately 80000 available nodes at the K computer) results in a computing time of 10 h on the K computer. Although each core at the Vienna Scientific Cluster operates at a faster clock speed of 2.7 GHz compared to the 2.0 GHz cores at the K computer, it is obvious that multiscale simulations for structurally complex materials like SiO_2 are feasible only on supercomputers of a size similar to the K computer.

Coupled simulations based on this framework have been performed previously [36, 37] to calculate the optical response, the energy deposition inside the material, and the ablation threshold. The results presented in this thesis aim at extending these preceding investigations. Previous results for SiO_2 exist and thus the study is restricted to this material. The simulated experimental setup was realized with the following parameters:

The laser pulse

- Pulse length $\tau_p = 12$ fs

- Intensity $I = 8.125 \times 10^{13} \text{ W/cm}^2$ ($\rightarrow I_{inside} = \sqrt{\frac{2}{1+n}} I \approx 5 \times 10^{13} \text{ W/cm}^2$)
- Carrier wavelength $\lambda = 730 \text{ nm}$
- Carrier-envelope phase $\phi_{CE} = \pi/2$
- Polarization direction $\mathbf{F}_0/|F_0| = \hat{\mathbf{z}}$ (compare Fig. 2.9)

The microscopic SiO_2 crystal cell

- Real space grid size $N_L = 20 \times 36 \times 50$
- Reciprocal space grid size $N_K \leq 4 \times 4 \times 4$
- Type of XC potential: TB-mBJ

The macroscopic setting

- 1D grid spacing $\Delta x = 250 \text{ a.u.} \approx 13.23 \text{ nm}$
- 1D grid size $N = 280$ (\rightarrow total material thickness of $d \approx 3.7 \mu\text{m}$)

In Fig. 4.1 the situation at the beginning of the simulation is depicted. As the charge transfer induced by the laser pulse along the laser polarization direction is investigated, the depth of the α -quartz layer must at least accommodate the complete laser pulse ($\tau_p c = 3.6 \mu\text{m}$), thereby avoiding the influence of reflections at the boundaries of the slab.

Figure 4.2 shows the electric field at $t = \tau_p$. While the reflected wave is a weak mirrored copy of the initial laser pulse travelling in the opposite direction, propagation of the pulse inside the material leads to a carrier-envelope phase shift and a compression of the pulse length due to chromatic dispersion originating from

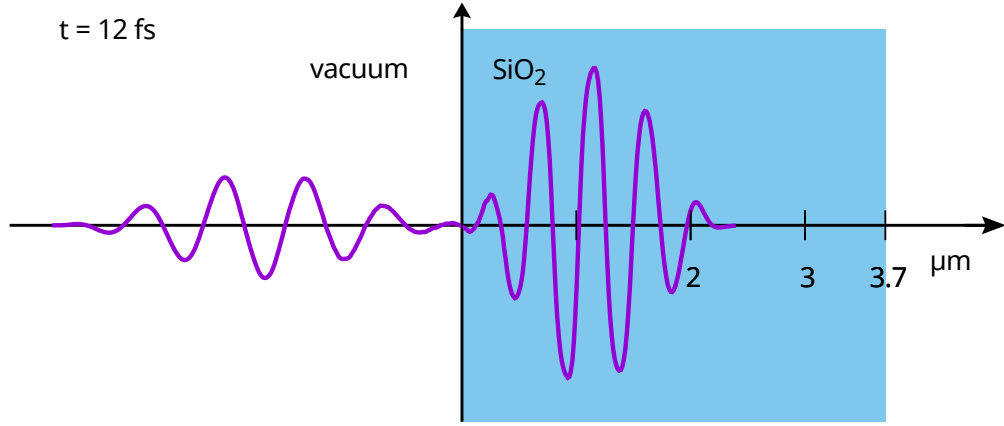


Figure 4.2: Electric field at $t = \tau_p = 12$ fs. Part of the laser pulse is reflected at the crystal surface. The transmitted wave shows a small phase shift towards the front of the pulse envelope and is compressed in length due to chromatic dispersion.

the frequency dependent refractive index. The spatial pulse length within the solid can be estimated with the help of the refractive index of SiO₂, $n(730 \text{ nm}) = 1.54$ [38], $\tau_p c/n = 2.34 \mu\text{m}$.

Deviations from the analytic solution of the Maxwell equations are only seen when analyzing the detailed structure of electric field $F(t)$ and polarization density $P(t)$ Fig. 4.3a in unit cells along the propagation direction. As expected, the amplitude of $F(t)$ is reduced as a function of penetration depth because the effects of coupling become more pronounced with increasing depth. Near the conclusion of the laser pulse (zoomed part of Fig. 4.3a) the electric field is distorted and does not vanish after the conclusion of the pulse but shows remaining fluctuations. While the maximum field strength is reduced at $x = 2 \mu\text{m}$ (yellow line) propagation effects induce a chirp of the pulse yielding an increase of the field strength during the last oscillation.

Figure 4.3b shows the polarization density for depths up to $2 \mu\text{m}$. Similar

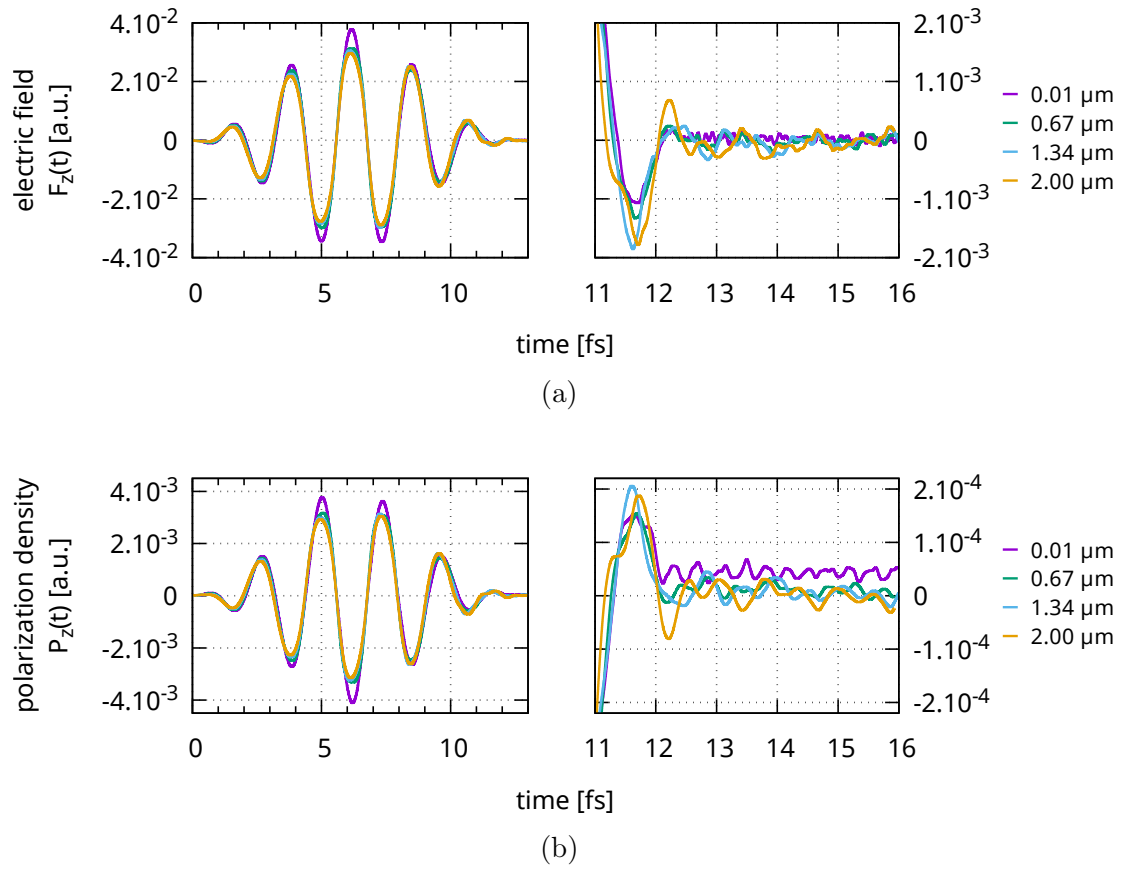


Figure 4.3: (a) Time-dependent electric field and (b) polarization density at different penetration depths. For better comparability $t = 0$ fs is shifted for each macroscopic point according to $t' = t + xn/c$.

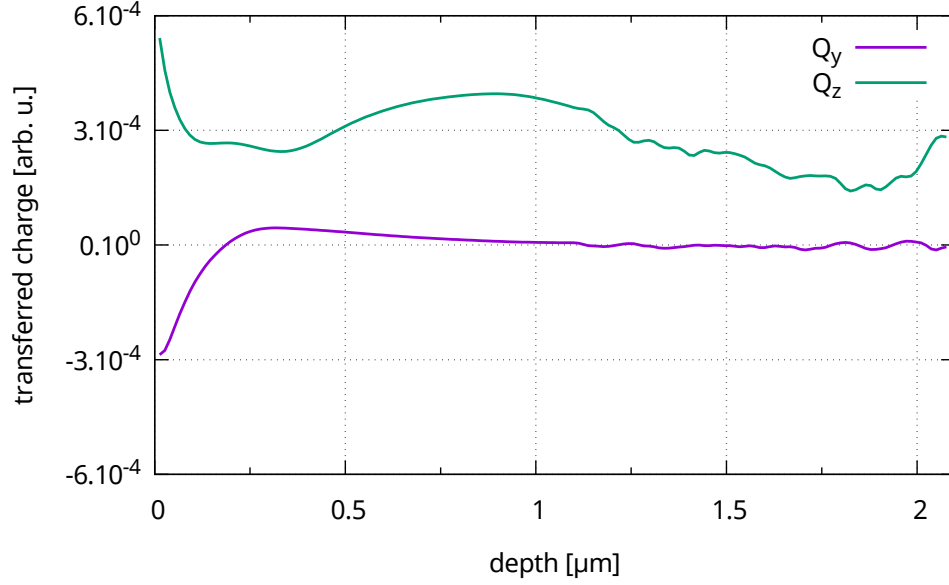


Figure 4.4: Macroscopic charge transfer within SiO_2 along the laser polarization direction z (green line) and an orthogonal direction y (purple line; x is the laser propagation direction).

to Fig. 3.5 the polarization density oscillates after the conclusion of the laser pulse for all positions but around a depth-dependent offset. Close to the surface of the crystal (purple and green lines) the polarization shows an average positive offset indicating a total charge transfer. This offset decreases with increasing depth.

For each macroscopic grid point the transferred charge can be calculated. Due to the various asymmetries of SiO_2 , not only currents in the polarization direction of the laser are induced but also in the two remaining spatial directions. In principle, currents in all directions should enter the solution of the Maxwell equations. However, such terms are not yet accounted for in our simulation and are regarded as vanishingly small contributions. That this condition is not always fulfilled can be clearly seen in Fig. 4.4 where the amount of transferred charge perpendicular to the polarization direction as function of the penetration depth is shown. Another

approximation employed in order to save computing time is the coarse grid in k -space. Grids with $2 \times 2 \times 2$, $2 \times 2 \times 4$, $2 \times 2 \times 8$, and $4 \times 4 \times 4$ points were tested and showed qualitatively completely different charge deposition characteristics. This is a strong hint that convergence was not yet reached for the finest employed grid and calls for further investigations. Either of these unsolved problems may furthermore be the reason for a small residual vector potential after the conclusion of the pulse which increases linearly with the penetration depth. Therefore, reliable results can not be presented so far but the problems have been identified and the following solutions can be proposed:

- Use only symmetric crystals (e.g. diamond) to circumvent the missing treatment of currents in the laser propagation direction and/or implement a full 3D solution of the Maxwell equations.
- Increase of the reciprocal grid size until convergence is reached.

5 Conclusions and outlook

In this thesis the effects appearing in bulk insulators due to irradiation with ultra-short high-intensity laser pulses were investigated. In particular, the electron dynamics on the (sub-)femtosecond timescale resulting in effective charge transfer inside the examined materials (α -quartz, diamond) were studied. Achieving control of this charge transfer by means of adjustable laser pulse parameters is of high interest for the development of new optically driven electronic signal processing devices.

The main method to achieve the presented results was time-dependent density functional theory. Comparison with experimental data has shown that TDDFT turned out to be a suitable method to describe microscopic processes within bulk insulators. Macroscopic transport phenomena were modeled based on coupling between models created for different scales, TDDFT and Maxwell's equations. This method turns out to be a powerful tool to investigate and understand surface and propagation effects. Complex systems, though, are very demanding in terms of computational resources. Therefore, semiclassical models for laser-matter interactions have been set up and have shown to enable qualitative predictions to facilitate estimations of the benefit of planned calculations.

As for silicon dioxide, an intensity dependent exponential increase of the trans-

ferred charge in laser polarization direction was found for diamond for ultra-short phase-stabilized laser pulses [32]. This increase appears due to a transition of the excitation mechanism from the multiphoton regime to the tunnel ionization regime. Along with the increasing transferred charge, a phase shift of the dependence on the carrier-envelope phase was confirmed, similar to former discoveries for electron emission from metal surfaces [35].

Asymmetries by the electric field can not only be introduced in the system employing carrier-envelope phase controlled ultra-short laser pulses but also by irradiating the target with two-color laser fields with controlled relative two-color phase or, equivalently, the easily controlled delay between the two components. For such systems an enhancement of the charge transfer by approximately one order of magnitude by variation of the two-color phase and the admixture of the second component was found.

Although the theoretical results of the simulations for diamond agree qualitatively with previously performed calculations for other materials, confirmation by comparison with experimental data is not yet possible due to a lack of results. The potential of two-color lasers to control the charge transfer has not yet been fully exploited. Further and more extensive studies of the parameter dependencies such as the mixing ratio have to be conducted and possibilities to improve the phase-dependent contrast of the transferred charge should be explored. Moreover, the multiscale approach is still in its infancy and allows for a rich amount of processes and phenomena to be studied. Challenges that have to be faced in order to enable further progress are the high demand in computational power and efficiency.

Acknowledgments

First of all, I would like to thank my advisor, *Christoph Lemell*, for granting me to carry out this thesis and for the combination of freedom and support he gave me throughout my research. His constructive objections and advices together with the vast experience and gut feeling of *Joachim Burgdörfer*, who also deserves many thanks, guided me in order to stay on track and make progress. Furthermore, without the introductory help and prior research of *Georg Wachter* I would not have been able to achieve my goals and therefore a great thank you also goes out to him. Special thanks go to *Kazuhiro Yabana*, *Xiao-Min Tong*, and *Shunsuke A. Sato* from the university of Tsukuba who invited me to Japan to deepen my knowledge about TDDFT and the simulation framework in use. Their hospitality and support as well as the beauty of the country of Japan left a strong impression on me.

Moreover, I am highly grateful for doing my thesis along with a remarkable colleague, *Isabella Floss*. Despite being busy with her own research, she never declined any calls for help and discussions and has always been a loyal and faithful fellow. Further thanks go out to my office colleagues, *Alexander Schumer* and *Valerie Smejkal*, for brightening up many days with vivid discussions not only about physics but also life in general.

This leads me to some more extensive acknowledgments. Without the huge support from my parents during the last seven years, whether it was of moral or financial form, I would certainly not have been able to finalize my studies. Thank you, *Maria* and *Johannes*, for the endless care and assistance I am allowed to experience on a daily basis. This also includes my gratitude towards their significant others, *Fritz* and *Magdalena*, and my sister *Elisabeth* for repeatedly drawing my attention back to the important things in life, including my newborn niece, *Hannah*.

Last but not least, the people I spent most of my time with during my studies deserve my utmost appreciation. Many of my physics-related insights are based on the profound conversations I had with my study colleagues. Besides that, the uncountable moments of fun and joy experienced with them, made this time an unforgettable one. Thank you, *Fabian Moisl*, *Johannes Brandstetter*, *Jakob Riedl*, *Markus Spanring*, *Jakob Fellingner*, *Philipp Moser* and *Thomas Madlener*, just to name a few.

Finally, special thanks go out to *Kerstin Höglinger*, a friend of incredible importance that stood besides me without regard of any circumstances. She has not only acted as a big source of motivation but also as someone who shed light on essential aspects of life which were new to me.

Bibliography

- [1] F. Krausz and M. I. Stockman. “Attosecond metrology: from electron capture to future signal processing”. *Nat. Phot.* 8.3 (2014). Review, pp. 205–213. DOI: 10.1038/nphoton.2014.28.
- [2] H. Childs et al. “VisIt: An End-User Tool For Visualizing and Analyzing Very Large Data”. *High Performance Visualization—Enabling Extreme-Scale Scientific Insight*. 2012, pp. 357–372.
- [3] Ferenc Krausz and Misha Ivanov. “Attosecond physics”. *Rev. Mod. Phys.* 81 (2009), pp. 163–234. DOI: 10.1103/RevModPhys.81.163.
- [4] K. Yabana et al. “Time-dependent density functional theory for strong electromagnetic fields in crystalline solids”. *Phys. Rev. B* 85 (2012), p. 045134. DOI: 10.1103/PhysRevB.85.045134.
- [5] P. Hohenberg and W. Kohn. “Inhomogeneous Electron Gas”. *Phys. Rev.* 136 (1964), B864–B871. DOI: 10.1103/PhysRev.136.B864.
- [6] W. Kohn and L. J. Sham. “Self-Consistent Equations Including Exchange and Correlation Effects”. *Phys. Rev.* 140 (1965), A1133–A1138. DOI: 10.1103/PhysRev.140.A1133.
- [7] J. P. Perdew and Alex Zunger. “Self-interaction correction to density-functional approximations for many-electron systems”. *Phys. Rev. B* 23 (1981), pp. 5048–5079. DOI: 10.1103/PhysRevB.23.5048.
- [8] F. Tran and P. Blaha. “Accurate Band Gaps of Semiconductors and Insulators with a Semilocal Exchange-Correlation Potential”. *Phys. Rev. Lett.* 102 (2009), p. 226401. DOI: 10.1103/PhysRevLett.102.226401.
- [9] J. P. Perdew and Y. Wang. “Accurate and simple analytic representation of the electron-gas correlation energy”. *Phys. Rev. B* 45 (1992), pp. 13244–13249. DOI: 10.1103/PhysRevB.45.13244.

-
- [10] A. D. Becke and E. R. Johnson. “A simple effective potential for exchange”. *The Journal of Chemical Physics* 124.22, 221101 (2006). DOI: 10.1063/1.2213970.
 - [11] A. D. Becke and M. R. Roussel. “Exchange holes in inhomogeneous systems: A coordinate-space model”. *Phys. Rev. A* 39 (1989), pp. 3761–3767. DOI: 10.1103/PhysRevA.39.3761.
 - [12] N. Troullier and J. L. Martins. “Efficient pseudopotentials for plane-wave calculations”. *Phys. Rev. B* 43 (1991), pp. 1993–2006. DOI: 10.1103/PhysRevB.43.1993.
 - [13] J. R. Chelikowsky, N. Troullier, and Y. Saad. “Finite-difference-pseudopotential method: Electronic structure calculations without a basis”. *Phys. Rev. Lett.* 72 (1994), pp. 1240–1243. DOI: 10.1103/PhysRevLett.72.1240.
 - [14] E. Runge and E. K. U. Gross. “Density-Functional Theory for Time-Dependent Systems”. *Phys. Rev. Lett.* 52 (1984), pp. 997–1000. DOI: 10.1103/PhysRevLett.52.997.
 - [15] R. van Leeuwen. “Mapping from Densities to Potentials in Time-Dependent Density-Functional Theory”. *Phys. Rev. Lett.* 82 (1999), pp. 3863–3866. DOI: 10.1103/PhysRevLett.82.3863.
 - [16] C. Ullrich. *Time-Dependent Density-Functional Theory: Concepts and Applications*. Oxford Graduate Texts. OUP Oxford, 2012. ISBN: 9780199563029.
 - [17] K. Yabana and G. F. Bertsch. “Time-dependent local-density approximation in real time”. *Phys. Rev. B* 54 (1996), pp. 4484–4487. DOI: 10.1103/PhysRevB.54.4484.
 - [18] L. V. Keldysh. “Ionization in the Field of a Strong Electromagnetic Wave”. *Sov. Phys. JETP* 20 (1965), pp. 1307–1314.
 - [19] S. H. Lin, A. A. Villaes, and Y. Fujimura. *Advances in Multi-Photon Processes and Spectroscopy*. Vol. 16. World Scientific, 2004. ISBN: 9789814481830.
 - [20] M. V. Ammosov, N. B. Delone, and V. P. Krainov. “Tunnel ionization of complex atoms and of atomic ions in an alternating electromagnetic field”. *Soviet Physics - JETP* 64.6 (1986), pp. 1191–1194.
 - [21] G. Wachter et al. “Controlling ultrafast currents by the nonlinear photogalvanic effect”. *New Journal of Physics* 17.12 (2015), p. 123026.
 - [22] S.M. Sze. *Semiconductor Devices: Physics and Technology*. Wiley, 1985, p. 20.

-
- [23] C. D. Clark, P. J. Dean, and P. V. Harris. “Intrinsic Edge Absorption in Diamond”. *Proceedings of the Royal Society of London A: Mathematical, Physical and Engineering Sciences* 277.1370 (1964), pp. 312–329. DOI: 10.1098/rspa.1964.0025.
- [24] L.S. Pan and D.R. Kania. *Diamond: Electronic Properties and Applications*. Electronic Materials: Science & Technology. Springer US, 2013. ISBN: 9781461522577.
- [25] E.D. Palik. *Handbook of Optical Constants of Solids*. Academic Press handbook series. Elsevier Science, 1998. ISBN: 9780080533780.
- [26] T. Nakatsukasa and K. Yabana. “Photoabsorption spectra in the continuum of molecules and atomic clusters”. *The Journal of Chemical Physics* 114.6 (2001), pp. 2550–2561. DOI: 10.1063/1.1338527.
- [27] K. Kihara. “An X-ray study of the temperature dependence of the quartz structure”. *European Journal of Mineralogy* 2.1 (1990), pp. 63–78. DOI: 10.1127/ejm/2/1/0063.
- [28] T.H. DiStefano and D.E. Eastman. “The band edge of amorphous SiO₂ by photoinjection and photoconductivity measurements”. *Solid State Communications* 9.24 (1971), pp. 2259–2261. DOI: 10.1016/0038-1098(71)90643-0.
- [29] J. R. Chelikowsky and M. Schlüter. “Electron states in α -quartz: A self-consistent pseudopotential calculation”. *Phys. Rev. B* 15 (1977), pp. 4020–4029. DOI: 10.1103/PhysRevB.15.4020.
- [30] E. Calabrese and W. B. Fowler. “Electronic energy-band structure of α quartz”. *Phys. Rev. B* 18 (1978), pp. 2888–2896. DOI: 10.1103/PhysRevB.18.2888.
- [31] H. R. Philipp. “Optical transitions in crystalline and fused quartz”. *Solid State Communications* 4 (1966), pp. 73–75. DOI: 10.1016/0038-1098(66)90109-8.
- [32] G. Wachter et al. “*Ab Initio* Simulation of Electrical Currents Induced by Ultrafast Laser Excitation of Dielectric Materials”. *Phys. Rev. Lett.* 113 (2014), p. 087401. DOI: 10.1103/PhysRevLett.113.087401.
- [33] C. Lemell et al. “Electron emission from surfaces induced by HCI and lasers”. *Nuclear Instruments and Methods in Physics Research Section B: Beam Interactions with Materials and Atoms* 235.1–4 (2005), pp. 425–430. DOI: 10.1016/j.nimb.2005.03.218.

-
- [34] P. Dombi et al. “Direct measurement and analysis of the carrier-envelope phase in light pulses approaching the single-cycle regime”. *New Journal of Physics* 6.1 (2004), p. 39.
 - [35] C. Lemell et al. “Electron Emission from Metal Surfaces by Ultrashort Pulses: Determination of the Carrier-Envelope Phase”. *Phys. Rev. Lett.* 90 (2003), p. 076403. DOI: 10.1103/PhysRevLett.90.076403.
 - [36] K.-M. Lee et al. “First-principles simulation of the optical response of bulk and thin-film α -quartz irradiated with an ultrashort intense laser pulse”. *Journal of Applied Physics* 115.5, 053519 (2014). DOI: 10.1063/1.4864662.
 - [37] S. A. Sato et al. “Time-dependent density functional theory of high-intensity short-pulse laser irradiation on insulators”. *Phys. Rev. B* 92 (2015), p. 205413. DOI: 10.1103/PhysRevB.92.205413.
 - [38] G. Ghosh. “Dispersion-equation coefficients for the refractive index and birefringence of calcite and quartz crystals”. *Optics Communications* 163.1–3 (1999), pp. 95–102. DOI: 10.1016/S0030-4018(99)00091-7.